

Raman microspectroscopy for microbiology

Kang Soo Lee^{1,a,†}, Zachary Landry^{1,a}, Fátima C. Pereira²,
Michael Wagner^{2,3}, David Berry², Wei E. Huang⁴, Gordon T. Taylor⁵,
Janina Kneipp⁶, Juergen Popp^{7,8}, Meng Zhang⁹, Ji-Xin Cheng⁹ and Roman Stocker^{1,†}

¹ Institute of Environmental Engineering, Department of Civil, Environmental and Geomatic Engineering, ETH Zurich, Zurich, Switzerland

² Division of Microbial Ecology, Department of Microbiology and Ecosystem Science, Centre for Microbiology and Environmental Systems Science, University of Vienna, Vienna, Austria

³ Department of Chemistry and Bioscience, Aalborg University, Aalborg, Denmark

⁴ Department of Engineering Science, University of Oxford, United Kingdom

⁵ School of Marine and Atmospheric Sciences, Stony Brook University, Stony Brook, USA

⁶ Department of Chemistry, Humboldt-Universität zu Berlin, Berlin, Germany

⁷ Institute of Physical Chemistry and Abbe Center of Photonics (ACP), Friedrich Schiller University Jena, Jena, Germany

⁸ Leibniz Institute of Photonics Technology e.V. Jena and Leibniz Health Technology, Jena, Germany

⁹ Department of Electrical and Computer Engineering & Department of Biomedical Engineering, Boston University, Boston, USA

October 2021

[†]Email: Kang Soo Lee (leeka@ethz.ch) and Roman Stocker (romanstocker@ethz.ch)

^aThese authors equally contributed to this work.

30 **Abstract**

31 Raman microspectroscopy offers microbiologists a rapid and non-destructive technique to assess the
32 chemical composition of individual live microorganisms in near real-time. In this Primer, we outline
33 the methodology and potential for its application to microbiology. We describe the technical aspects
34 of Raman analyses and practical approaches to apply this method to microbiological questions. We
35 discuss recent and potential future applications to determine the composition and distributions of
36 microbial metabolites down to subcellular scale; to investigate the host–microbe, cell–cell, and cell–
37 environment molecular exchanges that underlie the structure of microbial ecosystems from the ocean
38 to human gut microbiomes; and to interrogate the microbial diversity of functional roles in
39 environmental and industrial processes — key themes in modern microbiology. We describe the
40 current technical limitations of Raman microspectroscopy for investigation of microorganisms and
41 approaches to minimize or address them. Recent technological innovations in Raman
42 microspectroscopy will further reinforce the power and capacity of this method for broader adoptions
43 in microbiology, allowing microbiologists to deepen their understanding of the microbial ecology of
44 complex communities at nearly any scale of interest.

45

46 [H1] Introduction

47 Raman microspectroscopy is a form of vibrational spectroscopy that harnesses the inelastic scattering
48 of light, where the difference in wavelength between excitation and emission upon interaction with
49 the sample is determined by molecular vibration. This shift in wavelength provides information
50 about the molecular bonds present, and thus the chemical composition of the sample. Since the first
51 experimental observation of this scattering by C.V. Raman in 1928 (ref. ¹), Raman technology has
52 been widely adopted in materials science and engineering and is seeing growing applications in
53 microbiology and microbial ecology. Raman microspectroscopy represents a potentially game-
54 changing technology for our understanding of the diversity of metabolites and molecular interactions
55 underlying microbial ecology. Recent advances now enable in situ interrogation of the chemistry of
56 living microorganisms at sub-micrometre resolution. The technique is non-destructive, requires no
57 sample preparation and the measurement is simple and rapid, on the order of a few seconds per
58 measurement. The door is thus open to applications in microbiology for spatiotemporal probing of a
59 sample at single-cell scale (for typical micrometre-sized bacteria) or even subcellular scale (for larger
60 eukaryotic cells such as phytoplankton).

61
62 Raman technology is uniquely flexible compared to alternative methods with similar functionalities.
63 For example, **Fourier transform infrared (FTIR) spectroscopy [G]** suffers from strong absorption of
64 infrared wavelengths by water, hindering the use of the system to interrogate microbial cells in situ^{2,3}.
65 Nanoscale secondary ion mass spectrometry (nanoSIMS) and cryogenic electron microscopy (cryo-
66 EM) complemented with energy dispersive X-ray spectroscopy (EDS) enable much higher sensitivity
67 and spatial resolution than Raman microspectroscopy — down to a few tens of nanometres — but
68 require vacuum conditions and/or cryogenic temperatures for operation, making live-cell imaging
69 impossible⁴⁻⁹. Both approaches provide information on the elemental (and isotopic, in the case of
70 nanoSIMS) composition and structure of a sample, and not on its molecular composition. For
71 example, the amount of ¹³C compounds in a sample can be measured with nanoSIMS, yet their
72 distribution among molecules as part of lipids and storage compounds cannot be determined. The
73 ability of Raman systems to interrogate the chemistry of individual cells provides microbiologists a
74 means to rapidly investigate the ecophysiology of individual live microbes, offering for example an
75 opportunity to uncover the metabolic roles and contributions of microbes within complex
76 communities and to track metabolic exchange between microbial symbionts. For instance,
77 monitoring of carotenoids in autotrophic microalgae enables investigation of the photophysiology

78 under ecologically relevant conditions, such as through the diel cycle or under deficiency of
79 inorganic nutrients such as nitrogen, phosphorus, and silica¹⁰⁻¹⁷. Measuring ¹³C transfer from a host
80 to associated microbes (and vice versa) provides a means to interrogate the currency of carbon
81 exchange between the partners¹⁸. Despite this potential, Raman microspectroscopy is still
82 underutilized in microbiology.

83
84 This Primer aims to provide an overview of Raman technology and its potential applications for
85 microbiologists and bioengineers. We describe the fundamental principle and the advanced technical
86 add-ons of Raman microspectroscopy. Normal and resonance Raman microspectroscopy are the two
87 simplest modes of Raman microspectroscopy and are the main focus in this Primer, although we also
88 briefly discuss extended methods such as surface-enhanced Raman spectroscopy (SERS), hyper-
89 Raman, and coherent Raman **spectroscopy/microscopy [G]**. We outline criteria to optimize
90 experimental parameters and strategies to analyse the multivariate data that Raman
91 microspectroscopy provides, to extract accurate chemometric information about the sample. We
92 review applications in microbiology, which is currently maturing from examples in laboratory model
93 systems to the analysis of natural samples. Given that the majority of microbes on Earth are still not
94 cultivable, we then provide a roadmap for applying Raman technologies more widely to understand
95 the microbial ecology of complex communities in diverse real-world environments, such as
96 freshwater and oceans, soil, air and host-associated intestinal microbiomes. We discuss the current
97 technical limitations of Raman microspectroscopy for investigations of microbes and ways to
98 minimize and address these limitations. Finally, we outline possibilities to reinforce the power and
99 capacity of Raman microspectroscopy and to adopt the technique in underused fields in microbiology.

100 101 **[H1] Experimentation**

102 **[H2] *Raman working principles***

103 When a molecule encounters incident monochromatic light like from a coherent laser beam, it emits
104 light as a result of elastic scattering — known as Rayleigh scattering, where no wavelength shift
105 occurs after the interaction — and inelastic scattering — composed of Stokes and anti-Stokes Raman
106 scattering, where the emitted light has longer and shorter wavelengths, respectively, than the incident
107 light (**FIG. 1a**). These elastic and inelastic scattering are the result of excitation of the molecules to
108 virtual states and then a return to lower energy states with subsequent light emission (**FIG. 1c**).

109 **Normal Raman microspectroscopy [G]**, the most fundamental Raman system, usually relies on

110 Stokes Raman scattering. The magnitude of the shift in wavelength depends on the molecular
111 vibrational state, thus measuring the light emitted by a sample after excitation provides a means to
112 identify the molecular bonds present and hence the molecular composition of a sample. For example,
113 C–C bonds, the CH₂ group, and C double bonds with C or O induce shifts in wavenumber of 1,127,
114 1,304, and 1,665 cm⁻¹, respectively (FIG. 1b). When the wavelength of the incident laser beam
115 matches the electronic transitions of a molecule, the generated Raman signals are much greater (by a
116 factor of ~10³) than those from normal Raman microspectroscopy, an effect known as resonance
117 Raman scattering [G] (FIG. 1c). This is distinct from the fluorescence resulting from absorption —
118 fluorescence lifetimes (longer than nanoseconds) are much longer than in Raman scattering (on the
119 order of picoseconds).

120

121 [H2] *Variant Raman systems*

122 There have been various advances in Raman technology, particularly technical breakthroughs
123 addressing the limited sensitivity of normal Raman microspectroscopy. Technological advances
124 include, for example, UV and deep–UV resonance Raman spectroscopy, surface-enhanced Raman
125 spectroscopy (SERS), hyper-Raman spectroscopy (HRS), and coherent Raman scattering microscopy
126 (CRSM). These advances have fostered the adoption of Raman approaches in microbiology and
127 below we briefly describe the underlying working mechanisms, strengths, and important features of
128 these technologies. There are also many additional variant systems (such as tip-enhanced Raman
129 spectroscopy^{19,20} and spatially-offset Raman spectroscopy²¹), for which applications in microbiology
130 have not yet been demonstrated.

131

132 [H3] *UV and deep–UV resonance Raman spectroscopy*

133 A Raman laser with UV or deep–UV wavelengths (down to 200 nm) provides a means to interrogate
134 known metabolites of microbes with high sensitivity by virtue of resonance Raman scattering, which
135 does not occur in the visible or infrared wavelength range²². Additionally, the use of a short
136 wavelength laser further improves the sensitivity; Raman intensity is inversely proportional to the
137 laser wavelength to the power of four. Short wavelengths also improve diffraction-limited resolution
138 — the spatial resolution is proportional to the laser wavelength — reinforcing the capability of sub-
139 cellular Raman imaging of small bacterial cells. Despite these advantages^{23–27}, careful consideration
140 is required before adopting this technique for specific applications in which non-destructive sampling

141 is essential, since this wavelength region has a higher potential risk of laser-induced photo-damage
142 due to the resonance of the excitation laser with important cellular building blocks²⁸.

144 [H3] *Surface-enhanced Raman spectroscopy*

145 One can obtain Raman measurements with greatly improved sensitivity and selectivity by virtue of
146 surface-enhanced Raman scattering (SERS; further details can be found in refs. ^{29,30}), by bringing the
147 microorganism or molecule of interest into the vicinity of metallic nanoparticle substrates —
148 typically gold and silver with the size of a few tens of nanometres.

149
150 Several approaches can be considered when applying SERS to the investigation of microorganisms.
151 First, a plasmonic nanostructure can be designed and used as a SERS substrate. Physical contact or
152 close proximity of the SERS substrate with a cell enables measurement of the molecular composition
153 of the cell itself or of compounds that are secreted from the cell, respectively^{31,32} (**BOX 1**). In the
154 past two decades, several types of such SERS substrates have become commercially available, for
155 example, from [Horiba Scientific](#), [SERSitive](#), and many others. Second, metallic nanoparticles can be
156 applied to directly coat the cell surface or infiltrate across the bacterial cell envelope^{33–38}. Finally, a
157 SERS tag can be employed when aiming to identify cells with specific phenotypes or genotypes³⁹. In
158 one such approach, SERS tags consist of a metallic nanoparticle coated by a **Raman reporter [G]** and
159 then a layer of polyethylene glycol (PEG) or silica, which protects the Raman reporter layer from
160 surrounding stresses³⁹. The PEG or silica layer can be functionalized with antibodies or aptamers that
161 bind to specific microbes of interest. Compared to other SERS approaches, the use of SERS tags is
162 not limited by the need to achieve extremely close proximity of the nanoparticle surface to a cell of
163 interest, but it benefits from an optimized, efficient SERS enhancement — the SERS signals arise
164 from the Raman reporter engineered to be close to the nanoparticle, not from the cell itself.

166 [H3] *Hyper-Raman spectroscopy*

167 Hyper-Raman spectroscopy (HRS) relies on a nonlinear optical process (**FIG. 1c**; further details can
168 be found in ref. ⁴⁰). A **mode-locked laser [G]** with a near-infrared wavelength generates HRS signals
169 at visible wavelengths as if the excitation wavelength was half of the de facto excitation wavelength
170 — analogous to other two-photon processes, such as two-photon excited fluorescence⁴¹. The
171 generation of HRS signals depends on different **selection rules [G]** from other Raman scattering
172 based on one-photon processes, providing complementary molecular information about a sample. For

173 instance, HRS signals can reveal vibrations of molecules that are invisible to other Raman systems.
174 The signal intensity in HRS scattering is not high, and so sensitivity is boosted by combining HRS
175 with other techniques like SERS (known as surface-enhanced hyper-Raman spectroscopy; SEHRS^{42–}
176 ⁴⁴) or two-photon resonance with an electronic transition in a molecule (known as resonance HRS⁴⁰).

177 178 [H3] *Coherent Raman scattering microscopy*

179 Coherent Raman scattering microscopy (CRSM) provides the capability of rapid molecular imaging
180 (on the order of ~ 1 s for 200×200 pixels) at a selected wavenumber by virtue of 1,000-fold higher
181 sensitivity than normal Raman scattering (further details can be found in refs. ^{45,46}). It relies on
182 nonlinear optical processes arising from the interaction between two lasers: pump and Stokes lasers
183 with frequency ω_p and ω_s , respectively^{45–49}. Coherent anti-Stokes scattering (CARS) and stimulated
184 Raman scattering (SRS) result from this interaction. Briefly, CARS with a frequency $2\omega_p - \omega_s$ is
185 generated when the frequency difference between the pump and Stokes laser ($\omega_p - \omega_s$) is resonant
186 with a Raman-active molecular vibration in the sample (**Fig. 1c**). SRS is a dissipative process in
187 which the photon energy at a **beating frequency [G]** ($\omega_p - \omega_s$) is transferred from the pump laser
188 photons to the Stokes laser photons and then to a molecule in the sample, causing vibrational
189 excitation (**Fig. 1c**).

190
191 Coherent Raman scattering occurs at a specific wavenumber (at $2\omega_p - \omega_s$ and $\omega_p - \omega_s$ for CARS and
192 SRS, respectively) that can be adjusted by changing the wavelength of the pump laser (using a
193 tuneable laser source), while the wavelength of the Stokes laser is fixed (usually in infrared region;
194 around 1,045 nm). It is a powerful and sensitive tool enabling selective vibrational imaging of
195 microbes within a spatial region of interest with a resolution of ~ 350 nm, yet, unlike the other Raman
196 systems described above, the conditions generating a signal are specific to a specific wavenumber
197 and thus the technique does not lend itself to a comprehensive investigation of the molecular
198 composition of a sample across a broad Raman **spectral window [G]**. Recent innovations in the
199 technology are addressing this issue, such as multi-colour SRS^{50–52} which can simultaneously image
200 several wavenumber regions, and should lead to wider applications in microbiology.

201 202 [H2] *System configuration*

203 Raman systems for measurements of normal Raman scattering can be established on the basis of
204 several essential components: components for bright-field imaging to search for a region of interest

205 within a sample; a laser source to excite molecules within the sample to higher vibrational states;
206 optical components, including an objective, mirrors, beam splitters and a Rayleigh filter, to deliver
207 the laser beam onto the sample and the generated Raman signals back to the microspectroscopy
208 system, as well as to separate the polychromatic Raman signal by colour (known as **diffraction**
209 **grating [G]**); and a detector to measure Raman signals (**FIG. 2a**). Selection guidelines for technical
210 components to optimize Raman measurements for specific applications are discussed in **BOX 2**. To
211 use variant Raman systems, the system design must be adjusted accordingly. As an example, for UV
212 or deep-UV Raman spectroscopy, the optical components must be UV-compatible, while HRS
213 requires a mode-locked laser source for the generation of the two-photon process and CRSM needs a
214 two-colour laser to create the coherence effect and a lock-in amplifier to detect SRS signals.

215

216 To operate a Raman system, an imaging camera (camera 1; **FIG. 2a**), a motorized *xyz*-stage and
217 transmitted illumination (for example, bright-field microscopy) is first used to search for a spot of
218 interest within a sample and focus an excitation laser onto this spot. The camera is then deactivated
219 by removing a beam splitter during measurement to maximize the collection of generated Raman
220 signals. The transmitted illumination is also inactive during this step to avoid interference with the
221 measurements. In particular, if a light emitting diode (LED) is used for illumination, an anodized
222 optical shutter should be installed to prevent the Raman laser from travelling through the sample and
223 generating a signal from the LED unit. It is also important to note that the focal plane selected based
224 on visual inspection using camera 1 is usually not identical to that of the Raman laser due to
225 **chromatic aberration [G]**. The magnitude of this discrepancy depends on the specifications of the
226 objective. Before measurements of many samples are acquired, a depth profiling in the *z*-direction is
227 performed to determine the magnitude of the offset between the two foci for the particular objective
228 used — the position that provides maximum Raman intensities can be considered as the focus of the
229 Raman laser. When performing measurements, the microscope stage should be moved in the *z*-
230 direction by the distance of this offset after finding a spot of interest for Raman measurement using
231 bright-field microscopy.

232

233 During measurement, the width of the Raman laser beam is expanded using a beam expander to fully
234 fill the back aperture of the objective. The laser is delivered onto the sample and all backscattered
235 light is collected by the objective and returned to the spectrograph. A Rayleigh filter rejects Rayleigh
236 scattered signals, and the Raman signals generated from out-of-focus in the *z*-direction are blocked

237 by a confocal setup. Either a notch filter or an edge-pass filter can be used as the Rayleigh filter. We
238 recommend using an edge-pass filter — specifically, a long-pass or short-pass filter for the
239 measurement of Stokes or anti-Stokes Raman scattering, respectively — considering its nearly
240 infinite lifespan. Although a notch filter removes only the Rayleigh scattering and thus both Stokes
241 and anti-Stokes signals can be measured, it has a finite lifetime. In practice, an edge-pass filter often
242 produces wavy backgrounds — a non-zero baseline that is not flat across the spectrum. Measured
243 data should be corrected to separate molecular information about the sample from these
244 backgrounds⁵³. To this end, a calibration halogen lamp that generates a known Raman spectrum is
245 used (such as so-called ‘ICS correction’ using the halogen lamp for instruments from Horiba
246 Scientific).

247

248 Raman signals then pass through a slit and are collimated using a collimating mirror. A diffraction
249 grating separates the polychromatic scattered signals according to wavelength along the major axis of
250 the charge-coupled device (CCD) module arrays of a detector — module arrays arranged as a
251 rectangle are usually used for the Raman detector. Each CCD pixel measures the individual signals at
252 a different range of wavelengths. System calibration with respect to the strong Raman peak of a
253 commercial silicon wafer at 520.5 cm^{-1} (ref. ⁵⁴) is recommended every 24 hours or before every
254 experiment, since Raman measurements are influenced by environmental conditions such as
255 temperature.

256

257 For spatiotemporal interrogation of samples, two technical options can be considered: point
258 measurement or raster mapping of area or volume. In point measurement, Raman signals are
259 acquired from a single point at the focus of the Raman laser, such as from a single bacterium.
260 Typically, a point measurement with a high-power objective will have a resolution down to $0.3 \text{ }\mu\text{m}$,
261 depending on laser wavelength. The diffraction-limited spatial resolution is given by $1.22\lambda / \text{NA}$,
262 where λ and NA denote the laser wavelength and numerical aperture of the objective, respectively.
263 Raster mapping is possible through movement of the motorized *xyz*-stage, allowing interrogation of a
264 discretized array of points within an area or volume. This approach would allow for example the
265 measurement of a region of a biofilm matrix^{55,56} or a large microbial cell⁵⁷. To improve the speed of
266 area or volume measurements, a pair of scanning **galvomirrors [G]** (one for the *x*- and the other for
267 the *y*-axis) can be implemented in the position of the adjustable mirror (**FIG. 2b**). Compared to point

268 measurement, rapid area scanning provides a means to obtain comprehensive chemical information
269 from a sample that is larger than the spot size of the Raman laser beam.

271 [H2] *Integration with other optical systems*

272 A Raman system can be easily integrated with other optical components, thereby providing a means
273 to enhance the reliability and flexibility of Raman measurements and to obtain complementary
274 information (**FIG. 2b**). For example, optical tweezers^{58–60} can be implemented to allow precise and
275 reliable Raman measurement of small microbial cells by immobilizing a cell within the interrogation
276 volume during measurement⁶¹. Raman microspectroscopy is increasingly being used in combination
277 with epi-fluorescence microscopy. For example, fluorescence signals are recorded to identify
278 microbes of interest within a complex community using FISH (**BOX 3**) and Raman measurements
279 used to analyse their molecular composition⁶². For measurement of fluorescence signals, light of a
280 specific wavelength is directed onto the sample through a **dichroic mirror [G]**, and upon interaction
281 with fluorophores within the sample, the generated fluorescence signals travel back through an edge-
282 pass filter to a detector (camera 2). In general, Raman and fluorescence signals can be measured
283 from the same sample using fluorophores that are not excited by the Raman laser⁶³ or via
284 photobleaching techniques for fluorophores in which the excitation wavelength overlaps with that of
285 the Raman laser⁶². Raman and fluorescence measurements must be taken one after another because
286 the adjustable mirror needs to be withdrawn from the optical path to measure fluorescence signals.

288 [H2] *Sample preparation*

289 Samples can be measured in either dry or liquid form. To investigate time-dependent changes in the
290 ecophysiology of microbes, one can measure samples of dry cells taken from the population at
291 different time points, but the measurement of dry cell is destructive. To mitigate the risks of
292 physiological changes of cells before measurements, implementation of chemical fixation and
293 inactivation can be considered. Sodium azide or formaldehyde is recommended over other common
294 fixatives, such as glutaraldehyde or ethanol that could induce changes in the overall spectral
295 shape^{64,65}. Storing samples at <-80°C before measurements can alternatively be considered, but its
296 efficacy has not yet been quantitatively analysed. Alternatively, the ecophysiology of individual cells
297 can be tracked through time by measuring the same cells multiple times within a fluidic system
298 engineered to enable patterning of individual cells within an interrogation chamber based on physical
299 stamping of the cells on substrates or external force fields^{66,67}. We recommend to choose the former

300 approach for rapid measurements of cells with high sensitivity and the latter approach for
301 measurements of live cells with high reproducibility. In general, the sensitivity is higher with
302 measurements of dry cells due to the absence of interferences by Raman signals generated from a
303 liquid medium. Additionally, procedures for the preparations and measurements of dry cells are
304 straightforward; an example of these procedures can be found in ref. ⁶⁸. However, there is cell-to-cell
305 variation in background noise in measurements of dry cells — even within the same strain. Thus, to
306 allow quantitative comparison, data processing to remove this background is required (**FIG 3a**).

307
308 Cells in liquid phase generate reproducible Raman signals by virtue of a consistent level of signals
309 from the medium, although sensitivity can wane. Compared to measurements of dry cells, those in
310 liquid phase combined with a cell sorting platform^{61,63,69–72} provide an easier means to conduct
311 downstream analyses such as sequencing or cultivation of taxa of interest. Use of a liquid medium
312 provides a cooling effect, which mitigates the heating effect of the laser, and this cooling effect is
313 more pronounced with fluid flow. Dry samples will be more susceptible to laser-induced photo-
314 damage and thus require the use of a lower laser power. Signs of damage include a change in colour
315 to black due to combustion, physical disappearance of cells during measurement possibly due to
316 evaporation or cell lysis and abnormally high or saturated intensities in certain spectral regions,
317 depending on the wavelength of the laser.

318
319 When using liquid phase measurements, the choice of a non-photo-luminescent medium is important,
320 since signals from the medium could mask cellular signals. Samples incubated in photo-luminescent
321 media like LB medium should be re-suspended in an isotonic medium that does not induce osmotic
322 stress (for example, 0.2M glycerol balanced by Milli-Q), which increases the risk of photo-
323 damage^{61,63} (**FIG. 3b**). Additionally, Raman signals from water should be considered during
324 analysis^{61,63}. Specifically, an H₂O symmetric stretching peak at 1,665 cm⁻¹ interferes with
325 measurements of carbohydrate (C=C, C=O) and protein (amide I) signals (**Supplementary Table 1**)
326 and an OH peak at 3,400 cm⁻¹ coincides with strong lipid signals at 2,800–3,300 cm⁻¹ (ref. ⁷³).

327 328 [H3] *Stable isotope probing*

329 In microbiology one often seeks to quantify metabolic activity, growth and chemical transfers from
330 the environment to microbiota or among microorganisms. Incubation of a microbiome sample with
331 isotopically labelled compounds — known as stable isotope probing (SIP) — coupled to Raman

332 microspectroscopy can address a broad range of dynamical processes on a single-cell basis (reviewed
333 in ref. ⁷⁴).

334
335 The energy of Raman-scattered photons is largely controlled by the mass of the atoms involved in
336 the molecular vibration. A single additional neutron in an isotopically heavy tracer is sufficient to
337 slow a molecular vibration and lower the frequency of Raman-scattered photons from that of a
338 lighter **isotopologue [G]**. This phenomenon is observed as a red shift in the position of the peak
339 corresponding to the affected molecular bond. Principles behind spectral red shifts and factors
340 affecting their magnitude are explored in **Supplementary Note 2**.

341
342 Selection of an optimal isotope tracer for an experiment is driven primarily by the biological question
343 (**BOX 4**). Given that not all atoms in a substrate are necessarily assimilated into biomass, chances for
344 reliable detection and quantification are enhanced with substrates that have a **uniformly labelled**
345 **tracer [G]**. In laboratory SIP experiments, media can be engineered such that the tracer is a single
346 carbon source (like ¹³C-(U)-glucose or ¹³C-bicarbonate), a mixture of substrates (like ¹³C cellular
347 hydrolysates), a limiting nutrient (such as ¹⁵NH₄⁺) or a non-specific tracer of activity (like D₂O,
348 H₂¹⁸O)^{62,68,70,75-80}. In this case, tracer concentration and the medium's **fractional isotopic abundance**
349 **[G]** (f_{medium}) can be controlled. Knowing f_{medium} and the time-resolved measurements of fractional
350 isotopic abundances within cells (f_{cell}) enables computation of the absolute magnitude of the
351 assimilation of the substrate of interest into cell biomass, and thereby growth rates of individual
352 cells⁶⁸. In assessing in situ rates in environmental and microbiome samples, the tracer ideally would
353 not stimulate growth. To be detected by Raman microspectroscopy, however, stable isotope
354 substrates usually need to be added at non-tracer concentrations and as the dominant isotopologue of
355 a substrate of interest (for example, ¹³C-tracer concentration \gg in situ ¹²C-analogue concentration).
356 Thus, the tracer inflates the native substrate pool size and may stimulate activity⁶⁸. Experimental
357 design and interpretation must account for this potential artefact. In cases where f_{medium} cannot be
358 determined, valuable information can still be derived on relative activities among individual cells
359 from SIP incubations and also more generally about the flow of metabolites among cells and with the
360 environment.

361 **[H1] Results**

362 **[H2] Raman spectra**

364 A Raman spectrum is a multivariate data set that consists of discretized wavenumbers (x -axis) and
365 corresponding signal intensities (y -axis). Wavenumber (cm^{-1}) is the commonly used unit to represent
366 the Raman spectral shift from the laser excitation energy. The Raman shift (in cm^{-1}) is calculated as
367 $\Delta\nu = (1/\lambda_{\text{Inc}} - 1/\lambda_{\text{Scat}}) \times 10^7$, where λ_{Inc} and λ_{Scat} denote the wavelengths (in nm) of the incident and
368 scattered light, respectively, and the value 10^7 provides the conversion of the units from nm^{-1} to cm^{-1} .
369 The locations of peaks of interest within a Raman spectrum are independent of the wavelength of the
370 laser employed. For instance, the peak resulting from aromatic ring breathing for the amino acid
371 phenylalanine is located at $1,002\text{--}1,008 \text{ cm}^{-1}$ when a microbe is measured using either a 488 or a 532
372 nm laser. To interrogate the molecular composition of microorganisms, a spectral window of 700--
373 $3,400 \text{ cm}^{-1}$ is typically employed. This covers the **biomolecular fingerprints [G]** of microorganisms
374 ($<1,800 \text{ cm}^{-1}$; for example, carbohydrates, proteins, lipids, nucleic acids and carotenoids)²², a
375 **Raman-silent [G]** region ($1,800\text{--}2,700 \text{ cm}^{-1}$) in most (but not all) microbes and a carbon–deuterium
376 peak ($2,040\text{--}2,300 \text{ cm}^{-1}$) for SIP as well as CH stretching and water peaks ($>2,700 \text{ cm}^{-1}$).

377

378 Raman data are quasi-quantitative. Signal intensity at a given wavenumber is linearly proportional to
379 the concentration of the compound corresponding to that wavenumber, however signal intensity does
380 not provide an absolute value of the compound's concentration. Thus, changes in molecular
381 composition in different physiological, metabolic, or ecological states can in many cases be directly
382 evaluated by comparing intensities of the peaks⁸¹. To facilitate such comparisons between samples,
383 relative intensities should be used, taking the intensity of the signal of interest with respect to a
384 reference signal that is invariant with conditions and cell state, as absolute intensity values can vary
385 with variation in cell size and morphology⁷⁰, as well as sampled volume, which is sensitive to sample
386 opacity, thickness and focal plane. To relate signal intensities to absolute concentrations, independent
387 measurements should be used to generate a calibration curve^{68,81,82}. Within a spectrum, a molecule
388 corresponding to a strong peak cannot be considered to be more abundant than a molecule
389 corresponding to a weaker peak — a calibration curve for each peak must be generated.

390

391 To determine the identity of peaks within Raman spectra, there are currently two approaches. In a
392 first approach, published spectra or tables (or a commercial data library such as [KnowItAll](#)) listing
393 correspondences of biomolecules with spectral peaks can be used (**Supplementary Table 1**); we
394 recommend to use this approach as a priority. Alternatively, molecular identity can be established
395 using theoretical calculations. There are a number of commercial ([OptiFDTD](#)) and open-source

396 ([GAMESS](#), [ORCA](#)) tools that can estimate Raman emission values on the basis of quantum
397 mechanics. Albeit feasible, this has not been widely adopted for analyses of biological samples, as
398 many of these tools were optimized for pure solids. As Raman interrogations of biological samples
399 attract further interest, we expect that this approach will become more widely adopted. Spectral
400 peaks may not exactly match reported or calculated values as the wavelength shift can vary
401 somewhat depending on the precise configuration of the Raman microspectroscope and the presence
402 of side chains on molecules and inter-molecular interactions, thus care should be taken in interpreting
403 measured spectra. It is not straightforward to suggest acceptable margins, rather a comparison with
404 measurement of control samples (lacking in or abundant with chemical of interest) or pure chemical
405 of interest (commercially available or isolated from the sample) could confirm the identity of the
406 peaks of interest.

407

408 [H2] *Data processing*

409 Many Raman peaks are specific for a particular chemical moiety, thus data analysis can often be a
410 simple matter of tracking the magnitude of a peak of interest and can be carried out on the raw
411 spectra (**FIG. 4a**) or following a mild degree of pre-processing (such as de-noising only or
412 baseline subtraction). Raman spectra are also amenable to multivariate statistical analyses and
413 machine-learning approaches (also reviewed in refs. ^{83,84}). In the latter, accounting for
414 dimensionality and various sources of noise requires careful pre-processing to ensure high quality
415 data for repeatable downstream analyses. In particular, for analyses of dry cells, measurements are
416 often accompanied by considerable background, thus pre-processing is needed to allow
417 quantitative comparisons. It is essential that algorithms and parameters for the pre-processing are
418 identical for all data, otherwise quantitative comparisons are invalidated. Libraries for Raman data
419 processing (particularly pre-processing) can be found in **TABLE 1**.

420

421 [H3] *De-noising*

422 De-noising includes spectral smoothing and spike removal to prevent electronic noise or artefacts
423 (mainly arising from cosmic rays) from dominating measured Raman signals (**FIG. 4b,c**). The
424 most established approach to reduce spurious background noise is with application of the
425 **Savitzky–Golay filter [G]**^{85,86}. A related class of noise-reduction techniques relies on the fitting of
426 wavelet functions at each point in the spectrum, followed by subsequent soft thresholding⁸⁷. In
427 contrast to Savitzky–Golay, which uses a single polynomial, wavelet de-noising potentially

428 provides the ability to conduct spectral smoothing and spike removal simultaneously, and to
429 reduce noise at multiple levels of magnitude⁸⁸⁻⁹⁰. Dependency of its success on the specific choice
430 of wavelet and threshold parameters represents a potential downside⁸⁷.

431 [H3] *Baseline subtraction*

432 While not strictly necessary for many biological applications, baseline subtraction is useful to
433 eliminate large contaminating signals that originate from a number of sources, including the
434 instrument, the mounting substrate and the sample itself in the form of photo-luminescence. The
435 most commonly used approaches involve iteratively shrinking the intensities of the individual
436 columns of the spectrum via comparisons to an approximated curve (**FIG. 4d,e**). A popular group
437 of algorithms^{91,92} relies on the repeated fitting of a polynomial curve to the spectrum, followed by
438 subsequent clipping of larger peaks until the spectrum falls below a threshold value, then
439 subtracting the fitted polynomial from the original spectrum.
440

441
442 A related class of iterative fitting approaches is that of asymmetric least squares. This method
443 iteratively compares a spectrum to a version of itself that has been blurred via a sliding window
444 average, using a least squares fit. Each wavenumber is then progressively down-weighted using
445 separate weights for intensities above and below the fitted curve, with a bias against peaks
446 remaining above the blurred baseline⁹³. This approach is typically computationally faster and
447 simpler than polynomial fitting, while producing similar results, and thus may be better suited to
448 studies with a large number of spectra⁹³.

449 [H3] *Normalization and outlier removal*

450 Normalization of individual spectra is of value for any application where the intent is to compare
451 samples across different experiments, as small differences in instrument setup, substrate, and
452 sample preparation can greatly affect the intensity of the signal. Additionally, normalization is
453 useful when the relative intensity of the peaks is of interest for comparison among datasets, as
454 opposed to the absolute intensity. While there are many methods for normalizing multivariate
455 data⁹⁴, a straightforward approach that preserves the characteristic Raman spectral shape is **vector**
456 **normalization [G]**⁹⁵.
457

459 For analyses of large datasets, algorithms for outlier removal provide an efficient means to avoid
460 skewing of statistical results. In many cases, such as data influenced by fluorescence, outliers may
461 be obvious due to an extremely strong signal and may be discarded on the basis of predetermined
462 thresholds. In other cases, particularly where a large number of measurements are involved, it may
463 be beneficial to implement some form of automated outlier removal. Automated methods based on
464 Mahalanobis distance [G] have been used to successfully eliminate such outliers from large
465 Raman datasets⁹⁶.

466 [H3] *Classification of multivariate data*

468 Raman spectra are amenable to a variety of exploratory (unsupervised) or directed (supervised)
469 multivariate data analyses. The most familiar example of exploratory data analysis is principal
470 component analysis (PCA; FIG. 4f). PCA can be useful as an exploratory approach in itself or for
471 cursory inspection of major differences between samples. Similarly, the use of hierarchical clustering
472 or other simple clustering methods can also provide a good initial approximation of divisions within
473 the data. Slightly more advanced tools are related linear-decomposition/blind source separation
474 techniques such as non-negative matrix factorization [G]⁹⁷ and independent component analysis
475 [G]⁹⁸⁻¹⁰⁰ or unsupervised learning approaches such as self-organizing maps (SOM; FIG. 4g)¹⁰¹⁻¹⁰³,
476 each of which has been used in applications of Raman microspectroscopy to microbiology.

477
478 Supervised approaches can make use of simple classifiers^{104,105} or more advanced techniques, such as
479 artificial neural networks or random forest classifiers^{106,107}. These approaches are useful when
480 attempting to identify a particular known class of cells, material (like biofilm), or cellular metabolic
481 state. Simple classifiers such as support vector machines (SVM) and linear discriminant analysis
482 (LDA) are very effective at separating Raman data. These classifiers represent a good entry point for
483 researchers seeking to distinguish between one or more types of cells or biological materials. In its
484 simplest incarnation, using a linear kernel, a SVM (FIG. 4h) uses boundary points that are selected
485 from known groups of data to fit a separating hyperplane between classes of interest. In LDA (FIG.
486 4i), $(n-1)$ new axes are fitted to maximize the difference between (n) known (presumed Gaussian)
487 groups of data, while minimizing the variance among data within each group. To classify new data
488 points, typically a Bayesian approach¹⁰⁸ is used, assigning an identity to each point according to the
489 prior probabilities of each group along each linear discriminant.

491 A caveat to all classifier-based approaches is that they are entirely limited by the training data used.
492 As an example, classifiers have proven very successful at differentiating between single cells and
493 colonies for a number of strains of *Staphylococcus*^{106,109} based on Raman spectra, but are incapable
494 of making the same distinction for samples that contain new strains — those not reflected within the
495 training data — and would be prone to false positives as prior screening does not ensure that samples
496 fall within the currently defined outputs. Thus, training data needs to be carefully chosen beforehand,
497 with regard to the downstream application.

498

499 [H2] *Data interpretation*

500 In this section, we discuss best practice for analysing Raman data. In comparison with the previously
501 described techniques, where the wide spectral region is used as a whole to classify microbes or
502 molecules, we focus here on approaches to interpret the measured data on the basis of individual
503 peaks. We will outline six methods: identification of biomolecules based on normal Raman
504 microspectroscopy; measurement of resonance-inducing substances; SIP–Raman and FISH–Raman
505 for measurement of phenotypes (e.g., metabolic activities, functional roles within the community) or
506 identities (e.g., 16S rRNAs) of cells of interest, respectively, from within a complex microbial
507 community; measurements of biomolecules using SERS and SEHRS with increased sensitivity and
508 selectivity; and chemical imaging in terms of a specific wavenumber using CRSM.

509

510 [H3] *Identification of biomolecules*

511 A Raman spectrum of a single microbial cell provides a comprehensive biomolecular fingerprint
512 (representing, for example, nucleic acids, protein, lipids, carbohydrates; **Supplementary Table 1**),
513 reflecting the identity and metabolic physiology of the cell. Overall spectral shape within a broad
514 spectral region (700–3,400 cm⁻¹) can be used to differentiate among strains using supervised
515 machine-learning classifiers^{106,110,111}.

516

517 Alternatively, specific peaks can be used to investigate cells and their phenotypes of interest within a
518 complex microbial community. Here, we illustrate this approach using Raman spectra of *Bacillus*
519 *cereus*, a member of the phylum Firmicutes. When vegetative cells encounter harsh environmental
520 conditions such as desiccation or a lack of nutrients, they create a dormant endospore that germinates
521 when favourable conditions return¹¹². The formation of the endospore is accompanied by production
522 of calcium dipicolinic acid (CaDPA) and this can be detected in Raman spectra on the basis of

523 corresponding peaks at 824; 1,017; 1,395; 1,446; and 1,572 cm^{-1} (ref. ¹¹³). Endospores can be
524 distinguished from vegetative cells based on greater overall intensity in the spectrum (**FIG. 5a**),
525 possibly due to a denser biomass within the endospore. Alternatively, specific Raman peaks can be
526 used. For example, the height of the peak at 1,572 cm^{-1} becomes greater than the peak at 1,650 cm^{-1}
527 (corresponding to C=C and C=O bonds in diverse biochemicals) for the endospore. Additionally,
528 quantifying the height difference between these two peaks enables marking the process of entry to or
529 exit from dormancy of the cell.

530

531 [H3] *Resonance-inducing substances*

532 When microbes of interest contain molecules that can generate resonance Raman scattering (such as
533 carotenoids, cytochrome *c*, rhodopsins, haem proteins, flavin nucleotides and vitamin B₁₂) ^{76,114–119},
534 they can be measured with 1,000-fold higher sensitivity than normal Raman microspectroscopy.
535 Here, we use the analysis of carotenoid-containing microbes as an example. The carotenoids,
536 common pigments present in photoautotrophic microorganisms (and some heterotrophs¹²⁰), act as a
537 light-harvesting antenna at blue–green wavelengths and protect light-harvesting complexes¹²¹. Thus,
538 the ability to measure carotenoids provides a means to identify the microbes that participate in the
539 global carbon cycle. Carotenoids become resonant with a wide range of excitation wavelengths (from
540 UV to near-infrared) and three Raman peaks can be used to measure them (**FIG. 5b**): 1,001–1,007,
541 1,154–1,156, and 1,511–1,517 cm^{-1} , corresponding to C–CH₃ deformation, C–C stretching, and C=C
542 stretching, respectively. The peak at 1,511–1,517 cm^{-1} is the strongest, whereas the peak at 1,001–
543 1,007 cm^{-1} is often relatively weak compared to the other two (**FIG. 5c**). Measuring the intensity at
544 1,511–1,517 cm^{-1} enables the identification of carotenoid-containing cells from heterotrophs,
545 potentially followed by sorting of the cells for downstream analysis. The position of the peaks varies
546 depending on the type of carotenoid (such as fucoxanthin, beta-carotene or astaxanthin), thus, in
547 conjunction with measurements of commercially available pure carotenoids, the identity of
548 carotenoids in the cell can be determined. This approach is useful for many other Raman experiments.
549 Raman measurements of the pure chemicals of interest are necessary to confirm identification and
550 calibrate quantification. A trade-off is that a resonance Raman spectrum is dominated by the
551 resonance-inducing substances, thus optical¹²² or chemical¹²³ techniques bleaching those substances
552 must be considered to detect non-resonant biomolecules.

553

554 [H3] *SIP–Raman*

555 SIP experiments produce easily interpretable Raman spectra, providing an efficient means to
556 quantify microbial phenotypes of interest at single-cell level. For example, growing photoautotrophic
557 microorganisms in ^{13}C -bicarbonate for several hours and then measuring the red shift of Raman
558 signals from carotenoids allows quantification of cell growth rates and photophysiology (like
559 photosynthetic efficiency) with high sensitivity^{66,68}. The three carotenoids peaks are widened first to
560 lower wavenumbers with an increase in the level of ^{13}C -labelling and then shifted to lower
561 wavenumbers (**Fig. 5d**). For instance, the peak at $1,156\text{ cm}^{-1}$ (C–C stretching) moves to $1,133\text{ cm}^{-1}$
562 and then $1,110\text{ cm}^{-1}$ with the change from ^{12}C - ^{12}C to ^{13}C - ^{12}C and ^{13}C - ^{13}C . The approach for
563 quantification is described in ref. ⁶⁸. After bleaching the dominant carotenoid signals, other non-
564 resonant biomolecular signals can be revealed. We focus on the interpretation of red shifts in
565 phenylalanine peaks as a measure of carbon metabolism. Four sets of paired isotopomers [G] of ^{13}C -
566 labelled phenylalanine⁷⁷ (0, 2, 4 and 6 out of 6 ^{12}C within the aromatic ring are substituted by ^{13}C)
567 produce peaks at $1,002$ – $1,006$, 988 – 989 , 976 – 977 and 962 – 966 cm^{-1} , respectively (**FIG. 5e**). For
568 quantitative data analysis, a peak fitting approach can be applied using Voigt probability distribution
569 profiles [G]. Assuming that the ^{13}C fractional abundance in the phenyl ring is representative of all
570 cellular pools, then cellular fractional abundance (f_{cell}) can be calculated as $f_{\text{cell}} = (I_{966} + 0.67I_{977} +$
571 $0.33I_{988}) / (I_{966} + I_{977} + I_{988} + I_{1,002})$, where I represents Raman intensity at a wavenumber and
572 weighting factors 0.67 (2/3) and 0.33 (1/3) correspond to the number of ^{13}C atoms per isotopologue.

573

574 Limits of detection in SIP–Raman experiments vary among isotopes, tracer substrates, and detection
575 mode. For example, an f_{cell} of 0.10 (10 atom %) has been suggested as the limit of detection for
576 bacteria labelled with either ^{13}C or ^{15}N substrates when analysed using normal Raman
577 microspectroscopy⁷⁴. Detection by resonance Raman scattering has been shown to lower limits of
578 detection to an f_{cell} of 0.03 (3 atom %) for ^{13}C assimilated by photoautotrophs⁶⁸. For comparison,
579 nanoSIMS offers a significantly lower limit of detection ($f_{\text{cell}} = 0.001$; 0.1 atom %) for assimilated
580 ^{13}C ¹²⁴, but at significantly higher costs and lengthier analysis times as well as sacrificing the ability
581 to perform measurements of live cells.

582

583 SIP on the basis of deuterium labelling is another versatile approach to investigate the general
584 metabolic activities of microbes of interest from within a complex microbial community.

585 Measurement of f_{cell} in this case is even simpler, involving calculating the ratio of integrated

586 intensities under the C–D_x (2,040–2,300 cm⁻¹) and C–H_x (2,800–3,100 cm⁻¹) peak regions (**FIG.**
587 **4a**)^{69,70,78,125–127}.

588

589 [H3] *FISH–Raman*

590 FISH with rRNA-targeted oligonucleotide probes (**BOX 3**) can be used to identify cells of interest
591 within a complex microbial community and subsequent Raman measurements can quantify
592 functional properties of those cells⁶². Here, we use the example of naphthalene degraders
593 (*Acidovorax* spp. and *Pseudomonas* spp.) in groundwater biofilms¹²⁸. For FISH, probes for
594 *Acidovorax* spp., *Pseudomonas* spp., and all bacterial cells can be labelled using cyanine 3 (Cy3;
595 excitation/emission at 550/570 nm; red emission), fluorescein isothiocyanate (FITC; 495/518 nm;
596 green emission), and cyanine 5 (Cy5; 650/670 nm; purple emission), respectively, to allow them to
597 be differentiated in imaging using fluorescence microscopy (**FIG. 5f**). Following bleaching of
598 fluorescence to avoid interference with Raman measurement using a 532-nm laser, the level of
599 naphthalene degradation by each group of cells can be quantified using SIP–Raman (after
600 supplementing the medium with ¹³C–naphthalene), by calculating the intensity ratio $f_{\text{cell}} = I_{967} / I_{1,003}$
601 (**FIG. 5g,h**).

602

603 This FISH–Raman technique has been applied in many other systems, for example in investigations
604 of polyphosphate accumulating organisms (PAOs) in wastewater treatment plants^{81,129} and of the
605 composition of storage compounds in marine microbial consortia mediating anaerobic oxidation of
606 methane¹³⁰.

607

608 [H3] *SERS and SEHRS*

609 Interpretation of SERS spectra requires one to take into account the fact that metallic nanoparticles
610 used for SERS interact with molecules in a sample, which may create discrepancies in the number,
611 location and relative intensities of Raman peaks between normal Raman and SERS signals¹³¹. For
612 example, adenine has a strong Raman peak at 734 cm⁻¹ in SERS measurement¹³², whereas this peak
613 can be found at 721 cm⁻¹ in normal Raman spectra^{133,134}. Unlike in normal Raman spectra, when
614 charge, pH, or concentration of an analyte molecule changes, variation in the relative intensities of
615 spectral bands or the absence of vibrations of specific functional groups occurs due to the strong
616 dependence of the SERS enhancement on these parameters. Thus, care should be taken when

617 generating a calibration curve that is used to relate signal intensities to absolute concentrations of the
618 chemical¹³⁵.

619

620 Surface-enhanced hyper Raman spectroscopy (SEHRS) can complement SERS data. The generation
621 of SEHRS signals is governed by different selection rules, thus SEHRS can reveal peaks that are
622 relatively weak or not visible in SERS spectra. For example, adenine peaks at 564; 920; 1,141; 1,372;
623 and 1,464 cm^{-1} become intensified and peaks at 1,600 and 1,653 cm^{-1} , which are infrared-active,
624 become visible in SEHRS (FIG. 5i).

625

626 [H3] *CRSM*

627 CRSM imaging provides selective molecular information using an imaging modality that is similar to
628 optical microscopy imaging. To illustrate the approach, we use two stimulated Raman scattering
629 (SRS) images of deuterium-labelled *Pseudomonas aeruginosa* cells in blood (FIG. 5j), visualised
630 using protein (C–H; 2,915 cm^{-1}) and carbon–deuterium (C–D; 2,168 cm^{-1}) peaks. A 1,045 nm Stokes
631 laser is used and the pump laser is set at 801 and 852 nm, generating SRS signals at $(1/801 - 1/1,045)$
632 $\times 10^7 = 2,915 \text{ cm}^{-1}$ and $(1/852 - 1/1,045) \times 10^7 = 2,168 \text{ cm}^{-1}$, respectively. The SRS image based on
633 the C–D peak identifies the deuterium-labelled *P. aeruginosa* cells, whereas the blood cells are also
634 visualised in the image for the protein.

635

636 [H1] **Applications**

637 [H2] *Cellular metabolism and interactions*

638 [H3] *Cellular metabolism*

639 Measurement of storage compounds (such as lipids, polyhydroxyalkanoates, polyphosphate and
640 glycogen) within microbes is a very common application of Raman microspectroscopy in
641 microbiology^{81,130,136–145}. For example, this approach has been used to better understand mechanisms
642 of enhanced biological phosphorus removal in wastewater treatment plants^{81,138,139} and the
643 ecophysiology of uncultivated, subsurface-living ammonia-oxidizing archaea^{140,141} as well as
644 consortia mediating the anaerobic oxidation of methane¹³⁰.

645

646 Measurement of a wide variety of functional biomolecules (like carotenoids and cytochromes that
647 participate in photosynthesis, photoprotection and electron transfer within microorganisms; reviewed
648 in ref. ¹⁴⁶) and their states is another common use of Raman microspectroscopy. For instance,

649 cytochrome *c* and its oxidation state can be measured with high sensitivity by leveraging resonance
650 Raman scattering. This has been used to understand the metabolism of cable bacteria, a unique group
651 of multicellular, filamentous bacteria that inhabit sediments at the anoxic–oxic boundary¹⁴⁷. Raman
652 measurements have revealed that they have evolved a unique lifestyle by which they perform sulfide
653 oxidation and oxygen reduction at each end of their centimetre-long filaments in the anoxic and oxic
654 zones, respectively, based on the transport of electrons over this long distance¹⁴⁸.

655

656 The Raman spectrum of a cell reflects its physiological state. For example, measurement of ¹³C–
657 phenylalanine uptake by extracellular Chlamydia revealed that extracellular elementary bodies are in
658 fact metabolically active and synthesize proteins when they are transmitted between hosts. This
659 overturned an old dogma in which they were believed to be in a spore-like dormant state¹⁴⁹.

660

661 Raman microspectroscopy has also been used for measurements of the germination of dormant
662 endospores in situ¹⁵⁰. Time-resolved Raman measurements of individual endospore-forming
663 Firmicutes (in particular, *Bacillus thuringiensis*) have been achieved by trapping cells using optical
664 tweezers. Upon suspending the endospore powder in fresh, nutrient-rich medium, cells germinated
665 after 30 min of lag phase and rapidly released CaDPA into the surrounding medium (**FIG. 5a**).
666 Single-cell Raman measurements revealed cell-to-cell heterogeneity in time-to-germination, which
667 may be an important strategy at the population level that promotes survival when favourable
668 conditions are transient.

669

670 [H3] *Host–microbe, cell–cell, and cell–environment interactions*

671 In addition to the investigation of cellular metabolism, Raman measurements allow tracking of host–
672 microbe and intercellular interactions, providing insights into the functioning of these systems. One
673 example is the symbiosis between the flatworm *Paracatenula* and its alphaproteobacterial
674 endosymbiont, *Candidatus Riegeria*^{57,151}. It was long unclear how *Paracatenula*, a host lacking a
675 mouth and a digestive system, obtains energy. Raman imaging of *Ca. Riegeria* revealed a large
676 quantity of sulfur inclusions within the cell biomass, and metagenomics suggested that it gains
677 energy via sulfur oxidation, fuelling the bacteria and their host⁵⁷. Subsequent work using Raman
678 microspectroscopy showed that *Ca. Riegeria* also harbours polyhydroxyalkanoates and
679 carbohydrates that are transferred to the host via extracellular vesicles, serving as a primary energy
680 storage in the host¹⁵¹.

681
682 Raman imaging provides a powerful and non-invasive means to understand spatiotemporal and
683 metabolic interactions within complex microbial communities that determine community function
684 and macroscale processes in nature. For example, degradation of hyphae of the fungus *Mucor fragilis*
685 by the soil bacterium *Bacillus subtilis* has been investigated using SIP–Raman (in conjunction with
686 fluorescence imaging) based on ¹³C– and deuterium–labelling, imaged within a microfluidic device
687 containing a transparent soil microcosm¹⁵². Both planktonic cells and fungus-attached cells were
688 metabolically active when the system was hydrated, whereas fungus-attached cells were more active
689 under a dry-down/rewetting cycle, underlining the important role of fungi for the survival of bacteria
690 under fluctuating environmental conditions.

691
692 Raman imaging of the structure, chemical composition, and development of the biofilm matrix
693 provides another good example¹⁵³. Spectra can also be used to differentiate between co-localized
694 cells of the same species in multi-species consortia^{154–156}. For instance, measurements of the spatial
695 distribution of carotenoid-containing bacteria within a pink multi-species biofilm (commonly found
696 in household environments) revealed mutually exclusive distributions of different strains¹⁵⁷. The pink
697 biofilm is a potential pathogenic reservoir for immunocompromised patients and Raman imaging
698 could provide an efficient means to characterize this resistant matrix in situ.

699
700 Technical advances now enable visualisation of the chemical structure of biofilms with higher spatial
701 resolution and throughput than previously possible. Chemical imaging of calcium alginate fibres (a
702 model system for the biofilm matrix) with resolution of 20–50 nm has been achieved using tip-
703 enhanced Raman spectroscopy (TERS)¹³¹, and CRSM has allowed high-speed imaging (~7 s per
704 frame of 256 × 256 pixels) of biosynthesis of phenazines, which promote antibiotic tolerance, within
705 a *Pseudomonas aeruginosa* biofilm¹⁵⁸.

706 707 **[H2] Linking microbial functions to genes**

708 Integrating Raman microspectroscopy and a cell sorting method is a powerful approach to link the
709 phenotypes of microbes with their genotypes (**BOX 5**). In this approach, Raman microspectroscopy
710 is used to identify cells of interest with a specific phenotype (like metabolism or function) within a
711 complex community, often in conjunction with SIP, and a chip-based device like a microfluidic
712 device is used to situate cells within the Raman interrogation volume during measurement and

713 subsequently sort them on the basis of their spectra. The collected cells can be sequenced and the
714 recovered genomes used to link the identities and genetic makeups of the sorted cells to their
715 phenotypes. Samples can be kept in liquid media throughout this analysis process and thus the cells
716 of interest remain viable, enabling downstream cultivation for further ecological evaluation
717 (reviewed in refs. ^{159–161}).

718
719 The first application of Raman-based cell sorting combined with single-cell genomics revealed the
720 identity and gene content of uncultivated phototrophic bacteria from the ocean, part of what is known
721 as microbial dark matter¹¹⁶. Marine microbes were probed by Raman microspectroscopy for the
722 presence of carotenoid-containing chlorophyll or rhodopsin complexes, and target cells were sorted
723 using Raman-activated cell ejection (RACE; **BOX 5**). Despite the low number of sorted cells (27
724 cells) and low genome coverage (4.17–19.29%), this method enabled the identification of novel
725 carotenoid-containing bacteria, as well as novel functional genes involved in carotenoid and
726 isoprenoid biosynthesis¹¹⁶. In another study, RACE was used to identify microbes that contribute to
727 carbon fixation in the oceans¹¹⁷. Seawater samples from the sunlit ocean were spiked with
728 isotopically labelled ¹³C–bicarbonate and cells were ejected on the basis of resonant Raman bands
729 corresponding to carotenoids that displayed ¹³C-induced shifts (**FIG. 5d**). By sequencing groups of
730 approximately 30 ejected cells that were sorted and pooled together, complete genomes and
731 pathways for carotene synthesis as well as evidence for photosynthetic and anoxygenic CO₂ fixation
732 were recovered in two previously unknown *Synechococcus* sp. and *Pelagibacter* sp.¹¹⁷ (**FIG. 6a**). In
733 recent development of Raman-activated gravity-driven encapsulation and sequencing (RAGE–Seq;
734 **BOX 5**), high-quality single-cell genomes (>93% genome coverage) could be retrieved using
735 between a few and a hundred cells that were sorted from clinical (urogenital tract infection) and soil
736 microbiome samples^{71,162}.

737
738 Raman-based cell sorting has also been employed to study host-associated microbial communities
739 and to identify microorganisms of interest for therapeutic applications^{63,69,70} (**FIG. 6b**). To this end,
740 D₂O was used as a tracer to follow metabolically active cells from mouse gut communities that were
741 stimulated by supplementation with host-derived compounds, such as mucin or mucin-derived
742 mucosal sugars (**BOX 4** and **FIG. 4a**). Two different Raman-activated cell sorting (RACS) methods
743 (**BOX 5**) were then used to detect and sort D-labelled cells based on the presence of the specific C–D
744 Raman peak. In the first approach, cells were manually sorted and the collected cells lysed and

745 identified by 16S rRNA gene-targeted sequencing⁷⁰. With the recent development of high-throughput
746 RACS, it became possible to sort hundreds of cells of interest in a fully automated manner, and to
747 retrieve near-complete genomes of functionally active microbes, for example from gut
748 communities^{63,69}. This revealed the identity of mucin- and mucosal-sugar-foragers, such as
749 *Akkermansia*, *Allobaculum*, *Bacteroides*, *Barnesiella*, *Clostridiales*, and *Parabacteroides*^{69,70}. These
750 results were used to assemble a probiotic mixture with potential to counteract the gut pathogen
751 *Clostridioides difficile* through depletion of these sugars⁶⁹ (**FIG. 6b**). This example underscores the
752 value of RACS to identify microorganisms performing key functions within complex communities
753 like those in the gut, and how this information can be used to manipulate community functions.

754
755 Recent technological advances, such as the development of droplet-based sorters, have drastically
756 increased the throughput of Raman-based cell sorting, making it an attractive tool for
757 biotechnological applications^{72,163,164}. Rapid screening and selection of microbial cell factories that
758 efficiently produce compounds of interest is now performed using Raman-activated droplet
759 sorting^{72,164} (RADS; **BOX 5; FIG. 6c**). This approach has enabled sorting of cells of the alga
760 *Haematococcus pluvialis* able to produce large amounts of the commercially relevant antioxidant
761 carotenoid astaxanthin, with a throughput of 260 cells/min and >98% sorting accuracy¹⁶⁴. A
762 modified version of this platform (known as ‘pDEP–RADS’) allowed the rapid screening (120
763 cells/min; unlike RADS, this does not rely on measurements of resonance Raman scattering
764 generated from carotenoids) of cells of the yeast *Saccharomyces cerevisiae* accumulating microalgal
765 triacylglycerols, which are regarded as a potential renewable alternative to fossil fuels. The further
766 screening of a *S. cerevisiae* library expressing microalgal diacylglycerol acyltransferases followed by
767 sequencing of sorted cells led to identification of previously unknown enzymes able to produce the
768 monounsaturated fatty acid (MUFA)-rich triacylglycerols⁷² (**FIG. 6c**). Raman-based sorting can
769 thus streamline the selection of desirable microbial cell factories, and for example contribute to
770 achieving the high productivity required for microalgal biofuels to become economically feasible.

771

772 **[H2] Multiplexed identification of microbes**

773 Raman microspectroscopy has great potential in applications requiring the classification of a large
774 number of taxa, phenotypes or pathotypes based on chemical fingerprinting. We outline two
775 approaches: a label-free method (largely relying on machine learning) and barcoding of individual
776 microbes using SERS tags.

777

778 [H3] *A label-free approach*

779 Innovations in machine learning (in particular, supervised approaches) for the analysis of
780 multivariate data make this a useful means to classify taxa, phenotypes or pathotypes on the basis of
781 detection of small variations in their Raman spectra. The majority of biomolecules that are
782 measurable using Raman microspectroscopy are shared among taxa and thus the overall Raman
783 spectra are usually very similar with respect to the locations and number of peaks^{106,165}.

784 Classification is rarely possible by eye based on the spectral shape¹⁶⁶, thus software tools with high
785 discriminant ability are required. Supervised classifiers enable the detection of these small variations
786 and have been used to identify pathogens¹⁶⁷⁻¹⁷¹, to differentiate between pathogenic and non-
787 pathogenic *Escherichia coli* strains¹⁷², to discriminate between antibiotic-resistant *E. coli*
788 strains^{173,174} and to differentiate among species in situ within biofilm communities^{97,175}.

789

790 Two aspects must be considered in the use of supervised classifiers. First, Raman spectra are greatly
791 affected by the physiology of the microbes within a strain, such as heterogeneity in the metabolism
792 (for example, respiration vs. fermentation), growth state and biochemistry (like the ratio of proteins
793 to DNA)^{165,176,177}. Second, the measurements are influenced by the biotic and abiotic surroundings.
794 For instance, measurements of the same strain in urine, ascites, blood and soil are not identical. To
795 take these aspects into account, we recommend to: standardize conditions during sample preparation,
796 including medium, culturing time, pH, CO₂ concentration and diel cycle; establish a training
797 database containing the identical strains that will be used in real measurements and cross-validate it
798 using an independent test dataset; and where necessary, isolate cells of interest from peripheral biotic
799 and abiotic neighbours to minimize artefacts¹⁷⁸.

800

801 [H3] *Barcoding using SERS tags*

802 Use of a SERS tag that is conjugated with an antibody or aptamer enables selective attachment of the
803 tag to the targeted strain. Based on adoption of the technique in biomedical imaging (for example, in
804 vivo imaging of tumour cells¹⁷⁹), applications are expanding to biomedical microbiology, in
805 particular for the detection of pathogens using immunoassay platforms — devices that rely on an
806 antigen–antibody reaction^{180,181}. For example, *Staphylococcus aureus* and *Escherichia coli* O157:H7,
807 pathogens causing clinical diseases (like skin and respiratory infections) and foodborne poisoning,
808 have been detected in liquid samples using this approach (**FIG. 7**), and with enhanced sensitivity by

809 using device designs that enable spatial enrichment of the tagged cells based on dielectrophoresis or
810 magnetophoresis^{182–187}.

811
812 Compared to other technologies providing similar functionality (such as cultivation-based diagnosis
813 methods, PCR, and MALDI-TOF mass spectrometry¹⁸⁸), SERS tags provide a rapid (on the order of
814 a few minutes) and cultivation-free means for the multiplexed detection of microbes of interest. The
815 use of SERS tags that are synthesized using different chemicals for the Raman reporter layer and
816 then conjugated with different antibodies or aptamers enables targeted binding of these tags to
817 different strains and thereby multiplexed detection. Compared to the fluorescence-based tags that are
818 commonly used, SERS peaks have at least ten times narrower bandwidth and thus the number of
819 resolvable tags is increased accordingly. Despite this advantage, the technology has not yet reached
820 its full potential for multiplexing. SERS tags are potentially applicable in microbiology as an
821 alternative to fluorescence-based tags, for example, in genome-inferred antibody engineering —
822 known as reverse genomics¹⁸⁹. However, care should be taken in applying SERS tags for
823 measurement of intracellular compounds of some microorganisms as their relatively large size
824 (typically a few tens of nanometres) makes it difficult for them to penetrate cell walls or membranes.

825 826 **[H1] Reproducibility and data deposition**

827 There is currently no central, actively maintained repository for Raman spectra of biological and
828 organic compounds. To accompany this Primer, we are in the process of establishing a web-based
829 portal for the deposition of biological Raman data in a collaborative effort with the European
830 Molecular Biology Laboratory (EMBL) as part of the BioStudies initiative
831 (<http://www.ebi.ac.uk/biostudies>) — novel datasets can be submitted via the BioRaman template in
832 the BioStudies data submission tool. This platform will provide a means to accumulate Raman data
833 from diverse communities in microbiology and other fields of biology, and give full open access to
834 this data, along with the metadata necessary to facilitate reproducibility. We hope this portal will
835 provide an integrated and interactive resource similar to other established repositories for biological
836 data, enabling community access to data and the measurement procedures to plan future research,
837 and thereby stimulating to wider adoption of Raman technology in microbiology and biology as a
838 whole.

839 840 **[H2] *Minimum reporting standards***

841 Details of the spectra and their acquisition, including wavelength and power of the laser, laser
842 exposure time, the number of accumulations (for example, 3 if a measured spectrum was averaged
843 over three independent measurements), spectral resolution, specifications of the objective, the Raman
844 system used and measurement type (for example, normal Raman, resonance Raman or SERS) are
845 necessary. Other aspects of data treatment, as well as details concerning sample preparation and
846 mounting are also crucial. As a starting point, we have deposited five examples of Raman data
847 (formatted based on this minimum reporting standard) in the repository (also included in
848 **Supplementary File 2**): bacterial pure cultures of *Escherichia coli* (measurements of three samples
849 in liquid: ^{13}C - and deuterium-labelled, ^{13}C -labelled, and non-labelled) and *Vibrio alginolyticus*
850 (measurements of two dry samples: deuterium-labelled and not labelled; data used in **FIGS. 1b** and
851 **3a**); a xenic microalga culture of *Chaetoceros affinis* (measurements of two samples in liquid, ^{13}C
852 labelled and not labelled); a SRS image of deuterium-labelled *Pseudomonas aeruginosa* cells in
853 blood (data used in **FIG. 5j**¹³⁶); and a spectrum of the pure compound polyhydroxybutyrate.

854

855 **[H1] Limitations and optimizations**

856 **[H2] Sensitivity**

857 Normal Raman scattering has an inherently low quantum efficiency. To illustrate, laser-irradiated
858 samples scatter most photons elastically by Rayleigh scattering with no frequency shift (**FIG. 1a,c**).
859 Only about 1 in 10^6 of the laser's photons produces a Raman-scattered photon with frequency shifts.
860 Therefore, optimization of the instrument and sample preparation are essential to capture these
861 relatively rare scattering events. Recommendations for optimization and alternative methods for
862 signal amplification are presented above and in **Supplementary Note 1**. Efficient and reproducible
863 spectral processing is just as critical.

864

865 **[H2] Specificity**

866 Raman microspectroscopy is an incredibly powerful tool that provides structural fingerprints to
867 identify many specific molecules in compositionally simple samples like pure or nearly pure liquids,
868 crystals or gases. However, microorganisms are anything but compositionally simple and thus the
869 Raman spectra of cells often reveal little more than the presence of general classes of biomolecules.
870 A subset of specific compounds can routinely be identified from a single-cell spectrum, for example,
871 phenylalanine, adenine and thymine. When present in relatively high concentrations, storage
872 products¹⁹⁰, such as polyhydroxyalkanoates, polysaccharides, polyphosphates, sulphur inclusions,

873 and fatty acids, can also be easily identified from cellular Raman spectra^{122,190,191}. If highly abundant,
874 their spectral features may mask fingerprints of other cellular constituents of interest, thereby
875 complicating spectral interpretation. Recognition of many specific molecules within a cell is beyond
876 the reach of Raman microspectroscopy, because many different compounds share the same chemical
877 bond types and consequently share a vibrational mode. In addition, different bonds within the
878 complex cellular matrix can have overlapping vibrational energy distributions, resulting in broad
879 hybrid peaks that are challenging to disentangle. Therefore, careful selection of diagnostic molecules
880 and experimental conditions is essential to ensure meaningful and reproducible results as amply
881 demonstrated in studies described above.

882

883 **[H2] Fluorescence**

884 When present, laser-induced fluorescence produced by cellular **chromophores [G]** can overwhelm
885 normal Raman emissions, because fluorescence quantum efficiencies exceed those of normal Raman
886 scattering by orders of magnitude. Thus, Raman spectral features can be masked by broad and
887 intense fluorescence emissions over the entire Raman spectral range (see ref. ¹²³). This issue can be
888 resolved by multiple approaches, some of which require specific instrumentation or multiple lasers.
889 Most fluorescence avoidance or compensation methods capitalize on differences in the optical
890 behaviours of Raman and fluorescence excitation and emission radiation and are reviewed
891 elsewhere^{123,192}.

892

893 To address this issue using a standard confocal Raman microspectrophotometer, fluorescence can be
894 suppressed at a single spot or cell by exposure to a focused laser beam for a few minutes before
895 spectral acquisition⁶². However, using this approach for surveys of multiple targets in a single sample
896 can lead to unacceptably long data acquisition times. Prolonged data acquisition increases the
897 likelihood of both sample degradation and instrumental instabilities while hampering data throughput
898 and increasing analytical costs. Preparatory protocols (for example, chemiphoto-bleaching^{123,193,194})
899 that irreversibly suppress fluorescence in an entire biological sample can accelerate data acquisition.

900

901 **[H1] Outlook**

902 In this Primer, we have outlined approaches in contemporary Raman microspectroscopy, from
903 fundamental and advanced technical configurations, experimental considerations for successful
904 measurement of samples, to methodology for the handling and analysis of Raman data. We have also

905 provided an overview of the scope of potential applications in microbiology and microbial ecology,
906 such as interrogation of microbial metabolites, the biochemical currency of interactions between co-
907 existing partners, and identification of microbes performing functions of interest. We anticipate that,
908 by providing microbiologists with chemometric information at a scale relevant to microbes, Raman
909 microspectroscopy will become a breakthrough technology, opening a myriad of avenues of study
910 that will deepen our understanding of the physiology and ecology of the microbes populating the
911 complex microbial tree of life. With a growing community of microbiologists applying these
912 approaches to their work, we predict that Raman microspectroscopy may soon become the tool of
913 choice for certain aspects of microbiology.

914

915 There is of course significant room for further improvements. We here outline three directions that
916 hold promise in the near future.

917

918 **[H2] *Increasing sensitivity***

919 There are further opportunities to leverage recent innovations in Raman technology and apply them
920 as a way to interrogate cell ecophysiology and metabolic exchange between symbionts. The ability to
921 perform label-free, non-destructive and in situ measurements of samples is a unique and extremely
922 valuable feature of Raman microspectroscopy over alternative techniques like nanoSIMS⁴⁻⁷, cryo-
923 EM^{8,9} and fluorescence-based methods¹⁹⁵⁻¹⁹⁸. Raman measurements suffer from a lack of sensitivity
924 that stems directly from the nature of Raman scattering. To overcome this limitation, measurement of
925 dry samples has been used to enhance sensitivity, but with the loss of functionality from live cell
926 measurements. Advances in sensitivity resulting from improved detectors and resolution from the
927 super-resolution concept¹⁹⁹⁻²⁰¹ hold promise to enable investigation of extremely dilute bio-analytes.

928

929 State-of-the-art Raman systems can also contribute to resolving this issue. For example, time-gated
930 Raman spectroscopy²⁰² holds great potential, particularly for investigations of photoautotrophic
931 microorganisms and heterotrophs that contain resonance-inducing pigments, such as carotenoids. In
932 the presence of resonance-inducing substances, measurements of other cellular components are
933 typically masked by fluorescence signals that often accompany the resonance Raman scattering (**FIG.**
934 **5c**). Use of laser wavelengths that do not induce resonance is not always possible, and bleaching
935 techniques like hydrogen peroxide¹²³ sacrifice the ability to perform live cell interrogations. Time-
936 gated Raman microspectroscopy, by taking advantage of the time difference in the generation of

937 Raman and fluorescence signals^{203,204}, enables simultaneous measurements of resonance-inducing
938 substances via the accompanying fluorescence, as well as other non-resonant cellular compounds,
939 providing comprehensive molecular information for any type of microorganism.

940

941 **[H2] *Intelligent Raman***

942 In many fields, artificial intelligence is proving to be a game changer for handling data²⁰⁵. This is
943 also true in Raman microspectroscopy. Machine learning can provide an efficient means to detect
944 slight variation in spectral shape in series of time-resolved measurements or among measurements of
945 different species^{106,206-211}. Machine learning can also improve the precision and sensitivity of
946 conventional convolution/deconvolution methods to identify individual microorganisms or chemicals
947 within a spectrum in which multiple cells or compounds are simultaneously measured^{106,206-211}.

948

949 Comprehensive measurements of molecular composition of samples and identification of unknown
950 biochemical compounds may eventually become feasible. For example, there have been a few case
951 studies in which machine-learning platforms have been trained using Raman spectra of diverse types
952 of pathogenic bacteria, and were then able to successfully assign newly measured data to closed
953 related groups^{106,212,213}. On the contrary, Raman microspectroscopy has rarely been applied in
954 microbiology for naïve identification or measurement of unknown biochemical compounds. A likely
955 reason might be a lack of comparative data for biological Raman measurements, and partly to limited
956 sensitivity. In this regard, a central data repository should develop into a comprehensive database,
957 laying the foundations for improvement of identification techniques for diverse applications.

958

959 **[H2] *Adoption in unexploited fields***

960 The greatest strength of Raman microspectroscopy lies not in any specific aspect of the technology
961 itself, but in its versatile and robust nature. Bacteria live in a world in which chemical signals play a
962 predominant role in their ecology, and any approach that allows microbiologists to probe this world
963 in a dynamic fashion has enormous implications. There is huge potential for adoption of Raman
964 microspectroscopy in underexploited areas of environmental microbiology. For instance,
965 biomineralisation is a prime field for widespread adoption, as crystalline solids are often sources of
966 strong Raman scattering. Within this field, Raman has been used to profile a number of
967 mineralisation processes²¹⁴⁻²¹⁶ with consequences for nano- and biotechnology. Electro-microbiology,
968 an emerging field, has already applied Raman microspectroscopy in a unique and beautiful way to

969 confirm the ability of cable bacteria to couple the oxidation of sulfide to the reduction of oxygen over
970 long distances¹⁴⁸ and we expect more studies to follow. The study of environmental micro-plastics is
971 also especially well-suited to Raman microspectroscopic analyses²¹⁷, and cross-disciplinary research
972 addressing the role of microbes in the degradation of microplastics in the environment should see
973 further adoption^{218,219}.

974

975 While much microbiological research is currently limited to the laboratory, in the near future Raman
976 microspectroscopy could help establish coherent links between in situ field monitoring and more
977 closely controlled laboratory studies. Raman field samplers have already been successfully deployed
978 in diverse — and sometimes quite extreme — environments of microbial relevance. Automated
979 Raman profilers have been integrated into advanced oceanographic sampling equipment, such as
980 remotely operated vehicles (ROVs²²⁰), and deployed to hydrothermal vents²²¹. Raman profilers are
981 now standard equipment on unmanned space probes, with the technology currently integrated into
982 the European Space Agency's *Rosalind Franklin* and NASA's *Perseverance* Mars rovers^{22,222–226}.

983 These devices are being deployed with the express intent of looking for signatures of past or present
984 biological life in the form of cellular biomass²², large carbon deposits or high enantiomeric and
985 isotopic ratios in possible biogenic compounds, as one justification for their inclusion²²². Use of
986 these types of sensors in environmental monitoring applications is likely to greatly accelerate the
987 widespread adoption of Raman microspectroscopy by environmental microbiologists.

988

989 Additional biotechnological applications are already emerging in the booming field of synthetic
990 biology. As many synthetic biology approaches now rely, to some degree, on directed evolution^{227,228},
991 rapid screening of new cell lines for production of natural products or enhanced enzymatic activity is
992 increasingly important²²⁹. Much of this screening is currently being performed using labour-intensive
993 methods such as mass spectrometry. Due to its easy integration with other laboratory approaches, in
994 particular droplet microfluidics^{230–232}, Raman microspectroscopy provides distinct advantages in
995 methodology and cost.

996

997 Despite its long and established history in the physical sciences, it is possible that the age of utility
998 for Raman microspectroscopy is only just beginning. The continuing boom in new omics
999 technologies has given us the tools to map or identify nearly any latent feature potentially effecting
1000 microbially-controlled processes but there remains a dearth of techniques that allow us to investigate

1001 the actualization of these processes without destructive sampling or violent disruption of the sample.
1002 Raman microspectroscopy is unique not only in its broad utility as a tool for investigating chemical
1003 aspects of microbial metabolism, it stands (nearly) alone in its ability to do so in situ. From this
1004 standpoint alone, we predict that Raman microspectroscopy should see widespread adoption in the
1005 near future, particularly as technical aspects of the approach improve.

1007 References

- 1008 1. Raman, C. V. & Krishnan, K. S. A new type of secondary radiation. *Nature* **121**, 501–502 (1928).
- 1009 2. Baker, M. J. *et al.* Using Fourier transform IR spectroscopy to analyze biological materials. *Nat.*
1010 *Protoc.* **9**, 1771–1791 (2014).
- 1011 3. Movasaghi, Z., Rehman, S. & Rehman, I. U. Fourier transform infrared (FTIR) spectroscopy of
1012 biological tissues. *Appl. Spectrosc. Rev.* **43**, 134–179 (2008).
- 1013 4. Wagner, M. Single-cell ecophysiology of microbes as revealed by Raman microspectroscopy or
1014 secondary ion mass spectrometry imaging. *Annu. Rev. Microbiol.* **63**, 411–429 (2009).
- 1015 5. Li, T. *et al.* Simultaneous analysis of microbial identity and function using NanoSIMS. *Environ.*
1016 *Microbiol.* **10**, 580–588 (2008).
- 1017 6. Nuñez, J., Renslow, R., Cliff, J. B. & Anderton, C. R. NanoSIMS for biological applications: Current
1018 practices and analyses. *Biointerphases* **13**, 03B301 (2018).
- 1019 7. Musat, N., Foster, R., Vagner, T., Adam, B. & Kuypers, M. M. M. Detecting metabolic activities in
1020 single cells, with emphasis on nanoSIMS. *FEMS Microbiol. Rev.* **36**, 486–511 (2012).
- 1021 8. Weissenberger, G., Henderikx, R. J. M. & Peters, P. J. Understanding the invisible hands of sample
1022 preparation for cryo-EM. *Nat. Methods* **18**, 463–471 (2021).
- 1023 9. Oikonomou, C. M., Chang, Y.-W. & Jensen, G. J. A new view into prokaryotic cell biology from
1024 electron cryotomography. *Nat. Rev. Microbiol.* **14**, 205–220 (2016).
- 1025 10. Wakisaka, Y. *et al.* Probing the metabolic heterogeneity of live *Euglena gracilis* with stimulated
1026 Raman scattering microscopy. *Nat. Microbiol.* **1**, 16124 (2016).
- 1027 11. Barletta, R. E., Krause, J. W., Goodie, T. & El Sabae, H. The direct measurement of intracellular
1028 pigments in phytoplankton using resonance Raman spectroscopy. *Mar. Chem.* **176**, 164–173 (2015).
- 1029 12. Moudříková, Š. *et al.* Raman and fluorescence microscopy sensing energy-transducing and energy-
1030 storing structures in microalgae. *Algal Res.* **16**, 224–232 (2016).
- 1031 13. Heraud, P., Beardall, J., McNaughton, D. & Wood, B. R. *In vivo* prediction of the nutrient status of
1032 individual microalgal cells using Raman microspectroscopy. *FEMS Microbiol. Lett.* **275**, 24–30 (2007).
- 1033 14. Rüger, J. *et al.* Assessment of growth phases of the diatom *Ditylum brightwellii* by FT-IR and Raman
1034 spectroscopy. *Algal Res.* **19**, 246–252 (2016).
- 1035 15. Alexandre, M. T. A. *et al.* Probing the carotenoid content of intact *Cyclotella* cells by resonance
1036 Raman spectroscopy. *Photosynth. Res.* **119**, 273–281 (2014).
- 1037 16. Premvardhan, L., Bordes, L., Beer, A., Büchel, C. & Robert, B. Carotenoid structures and
1038 environments in trimeric and oligomeric fucoxanthin chlorophyll a/c₂ proteins from resonance Raman
1039 spectroscopy. *J. Phys. Chem. B* **113**, 12565–12574 (2009).
- 1040 17. Büchel, C. How diatoms harvest light. *Science* **365**, 447–448 (2019).
- 1041 18. Dolinšek, J., Lagkouvardos, I., Wanek, W., Wagner, M. & Daims, H. Interactions of nitrifying bacteria
1042 and heterotrophs: identification of a *Micavibrio*-like putative predator of *Nitrospira* spp. *Appl. Environ.*
1043 *Microbiol.* **79**, 2027–2037 (2013).
- 1044 19. Shao, F. & Zenobi, R. Tip-enhanced Raman spectroscopy: principles, practice, and applications to
1045 nanospectroscopic imaging of 2D materials. *Anal. Bioanal. Chem.* **411**, 37–61 (2019).
- 1046 20. Yeo, B.-S., Stadler, J., Schmid, T., Zenobi, R. & Zhang, W. Tip-enhanced Raman Spectroscopy – Its
1047 status, challenges and future directions. *Chem. Phys. Lett.* **472**, 1–13 (2009).
- 1048 21. Mosca, S., Conti, C., Stone, N. & Matousek, P. Spatially offset Raman spectroscopy. *Nat. Rev.*

- 1049 *Methods Prim.* **1**, 21 (2021).
- 1050 22. Sapers, H. M. *et al.* The cell and the sum of its parts: patterns of complexity in biosignatures as
1051 revealed by deep UV Raman spectroscopy. *Front. Microbiol.* **10**, 679 (2019).
- 1052 23. Nelson, W. H., Manoharan, R. & Sperry, J. F. UV resonance Raman studies of bacteria. *Appl.*
1053 *Spectrosc. Rev.* **27**, 67–124 (1992).
- 1054 24. Wu, Q. *et al.* UV Raman spectral intensities of *E. coli* and other bacteria excited at 228.9, 244.0, and
1055 248.2 nm. *Anal. Chem.* **73**, 3432–3440 (2001).
- 1056 25. Jarvis, R. M. & Goodacre, R. Ultra-violet resonance Raman spectroscopy for the rapid discrimination
1057 of urinary tract infection bacteria. *FEMS Microbiol. Lett.* **232**, 127–132 (2004).
- 1058 26. Žukovskaja, O. *et al.* UV-Raman spectroscopic identification of fungal spores important for respiratory
1059 diseases. *Anal. Chem.* **90**, 8912–8918 (2018).
- 1060 27. Boustany, N. N., Manoharan, R., Dasari, R. R. & Feld, M. S. Ultraviolet resonance Raman
1061 spectroscopy of bulk and microscopic human colon tissue. *Appl. Spectrosc.* **54**, 24–30 (2000).
- 1062 28. Kumamoto, Y., Taguchi, A., Smith, N. I. & Kawata, S. Deep ultraviolet resonant Raman imaging of a
1063 cell. *J. Biomed. Opt.* **17**, 076001 (2012).
- 1064 29. Kneipp, J., Kneipp, H. & Kneipp, K. SERS—a single-molecule and nanoscale tool for bioanalytics.
1065 *Chem. Soc. Rev.* **37**, 1052–1060 (2008).
- 1066 30. Langer, J. *et al.* Present and future of surface-enhanced Raman scattering. *ACS Nano* **14**, 28–117
1067 (2020).
- 1068 31. Lussier, F. *et al.* Dynamic-SERS optophysiology: A nanosensor for monitoring cell secretion events.
1069 *Nano Lett.* **16**, 3866–3871 (2016).
- 1070 32. Caprettini, V. *et al.* Enhanced Raman investigation of cell membrane and intracellular compounds by
1071 3D plasmonic nanoelectrode arrays. *Adv. Sci.* **5**, 1800560 (2018).
- 1072 33. Efrima, S. & Bronk, B. V. Silver colloids impregnating or coating bacteria. *J. Phys. Chem. B* **102**,
1073 5947–5950 (1998).
- 1074 34. Zhou, H. *et al.* SERS detection of bacteria in water by in situ coating with Ag nanoparticles. *Anal.*
1075 *Chem.* **86**, 1525–1533 (2014).
- 1076 35. Drescher, D., Traub, H., Büchner, T., Jakubowski, N. & Kneipp, J. Properties of *in situ* generated gold
1077 nanoparticles in the cellular context. *Nanoscale* **9**, 11647–11656 (2017).
- 1078 36. Palanco, M. E. *et al.* Templated green synthesis of plasmonic silver nanoparticles in onion epidermal
1079 cells suitable for surface-enhanced Raman and hyper-Raman scattering. *Beilstein J. Nanotechnol.* **7**,
1080 834–840 (2016).
- 1081 37. Weiss, R. *et al.* Surface-enhanced Raman spectroscopy of microorganisms: Limitations and
1082 applicability on the single-cell level. *Analyst* **144**, 943–953 (2019).
- 1083 38. Premasiri, W. R. *et al.* The biochemical origins of the surface-enhanced Raman spectra of bacteria: a
1084 metabolomics profiling by SERS. *Anal. Bioanal. Chem.* **408**, 4631–4647 (2016).
- 1085 39. Wang, Y., Yan, B. & Chen, L. SERS tags: Novel optical nanoprobe for bioanalysis. *Chem. Rev.* **113**,
1086 1391–1428 (2013).
- 1087 40. Kelley, A. M. Hyper-Raman scattering by molecular vibrations. *Annu. Rev. Phys. Chem.* **61**, 41–61
1088 (2010).
- 1089 41. Helmchen, F. & Denk, W. Deep tissue two-photon microscopy. *Nat. Methods* **2**, 932–940 (2005).
- 1090 42. Madzharova, F., Heiner, Z. & Kneipp, J. Surface enhanced hyper Raman scattering (SEHRS) and its
1091 applications. *Chem. Soc. Rev.* **46**, 3980–3999 (2017).
- 1092 43. Kneipp, J., Kneipp, H. & Kneipp, K. Two-photon vibrational spectroscopy for biosciences based on
1093 surface-enhanced hyper-Raman scattering. *Proc. Natl. Acad. Sci. U. S. A.* **103**, 17149–17153 (2006).
- 1094 44. Heiner, Z., Gühlke, M., Živanović, V., Madzharova, F. & Kneipp, J. Surface-enhanced hyper Raman
1095 hyperspectral imaging and probing in animal cells. *Nanoscale* **9**, 8024–8032 (2017).
- 1096 45. Zhang, C., Zhang, D. & Cheng, J.-X. Coherent Raman scattering microscopy in biology and medicine.
1097 *Annu. Rev. Biomed. Eng.* **17**, 415–445 (2015).
- 1098 46. Min, W., Freudiger, C. W., Lu, S. & Xie, X. S. Coherent nonlinear optical imaging: Beyond
1099 fluorescence microscopy. *Annu. Rev. Phys. Chem.* **62**, 507–530 (2011).
- 1100 47. Zhang, D., Wang, P., Slipchenko, M. N. & Cheng, J.-X. Fast vibrational imaging of single cells and
1101 tissues by stimulated Raman scattering microscopy. *Acc. Chem. Res.* **47**, 2282–2290 (2014).

- 1102 48. Freudiger, C. W. *et al.* Label-free biomedical imaging with high sensitivity by stimulated Raman
1103 scattering microscopy. *Science* **322**, 1857–1861 (2008).
- 1104 49. Yue, S. & Cheng, J.-X. Deciphering single cell metabolism by coherent Raman scattering microscopy.
1105 *Curr. Opin. Chem. Biol.* **33**, 46–57 (2016).
- 1106 50. Suzuki, Y. *et al.* Label-free chemical imaging flow cytometry by high-speed multicolor stimulated
1107 Raman scattering. *Proc. Natl. Acad. Sci. U. S. A.* **116**, 15842–15848 (2019).
- 1108 51. De la Cadena, A., Valensise, C. M., Marangoni, M., Cerullo, G. & Polli, D. Broadband stimulated
1109 Raman scattering microscopy with wavelength-scanning detection. *J. Raman Spectrosc.* **51**, 1951–
1110 1959 (2020).
- 1111 52. Lu, F.-K. *et al.* Multicolor stimulated Raman scattering microscopy. *Mol. Phys.* **110**, 1927–1932
1112 (2012).
- 1113 53. Choquette, S. J., Etz, E. S., Hurst, W. S., Blackburn, D. H. & Leigh, S. D. Relative intensity correction
1114 of Raman spectrometers: NIST SRMs 2241 through 2243 for 785 nm, 532 nm, and 488 nm/514.5 nm
1115 excitation. *Appl. Spectrosc.* **61**, 117–129 (2007).
- 1116 54. Sui, Z., Leong, P. P., Herman, I. P., Higashi, G. S. & Temkin, H. Raman analysis of light-emitting
1117 porous silicon. *Appl. Phys. Lett.* **60**, 2086–2088 (1992).
- 1118 55. Ivleva, N. P., Wagner, M., Horn, H., Niessner, R. & Haisch, C. Raman microscopy and surface-
1119 enhanced Raman scattering (SERS) for in situ analysis of biofilms. *J. Biophotonics* **3**, 548–556 (2010).
- 1120 56. Ivleva, N. P., Kubryk, P. & Niessner, R. Raman microspectroscopy, surface-enhanced Raman
1121 scattering microspectroscopy, and stable-isotope Raman microspectroscopy for biofilm
1122 characterization. *Anal. Bioanal. Chem.* **409**, 4353–4375 (2017).
- 1123 57. Gruber-Vodicka, H. R. *et al.* *Paracatenula*, an ancient symbiosis between thiotrophic
1124 *Alphaproteobacteria* and catenulid flatworms. *Proc. Natl. Acad. Sci. U. S. A.* **108**, 12078–12083
1125 (2011).
- 1126 58. Bustamante, C. J., Chemla, Y. R., Liu, S. & Wang, M. D. Optical tweezers in single-molecule
1127 biophysics. *Nat. Rev. Methods Prim.* **1**, 25 (2021).
- 1128 59. Ashkin, A. & Dziedzic, J. M. Optical trapping and manipulation of viruses and bacteria. *Science* **235**,
1129 1517–1520 (1987).
- 1130 60. Ashkin, A. Forces of a single-beam gradient laser trap on a dielectric sphere in the ray optics regime.
1131 *Biophys. J.* **61**, 569–582 (1992).
- 1132 61. Lee, K. S. *et al.* Optofluidic Raman-activated cell sorting for targeted genome retrieval or cultivation
1133 of microbial cells with specific functions. *Nat. Protoc.* **16**, 634–676 (2021).
- 1134 62. Huang, W. E. *et al.* Raman-FISH: Combining stable-isotope Raman spectroscopy and fluorescence *in*
1135 *situ* hybridization for the single cell analysis of identity and function. *Environ. Microbiol.* **9**, 1878–
1136 1889 (2007).
- 1137 63. Lee, K. S. *et al.* An automated Raman-based platform for the sorting of live cells by functional
1138 properties. *Nat. Microbiol.* **4**, 1035–1048 (2019).
- 1139 64. Read, D. S. & Whiteley, A. S. Chemical fixation methods for Raman spectroscopy-based analysis of
1140 bacteria. *J. Microbiol. Methods* **109**, 79–83 (2015).
- 1141 65. García-Timmermans, C. *et al.* Label-free Raman characterization of bacteria calls for standardized
1142 procedures. *J. Microbiol. Methods* **151**, 69–75 (2018).
- 1143 66. Behrendt, L. *et al.* PhenoChip: A single-cell phenomic platform for high-throughput
1144 photophysiological analyses of microalgae. *Sci. Adv.* **6**, eabb2754 (2020).
- 1145 67. Collins, D. J. *et al.* Two-dimensional single-cell patterning with one cell per well driven by surface
1146 acoustic waves. *Nat. Commun.* **6**, 8686 (2015).
- 1147 68. Taylor, G. T. *et al.* Single-cell growth rates in photoautotrophic populations measured by stable isotope
1148 probing and resonance Raman microspectrometry. *Front. Microbiol.* **8**, 1449 (2017).
- 1149 69. Pereira, F. C. *et al.* Rational design of a microbial consortium of mucosal sugar utilizers reduces
1150 *Clostridiodes difficile* colonization. *Nat. Commun.* **11**, 5104 (2020).
- 1151 70. Berry, D. *et al.* Tracking heavy water (D₂O) incorporation for identifying and sorting active microbial
1152 cells. *Proc. Natl. Acad. Sci. U. S. A.* **112**, E194–E203 (2015).
- 1153 71. Xu, T. *et al.* Phenome–genome profiling of single bacterial cell by Raman-activated gravity-driven
1154 encapsulation and sequencing. *Small* **16**, 2001172 (2020).

- 1155 72. Wang, X. *et al.* Positive dielectrophoresis-based Raman-activated droplet sorting for culture-free and
1156 label-free screening of enzyme function in vivo. *Sci. Adv.* **6**, eabb3521 (2020).
- 1157 73. Czamara, K. *et al.* Raman spectroscopy of lipids: a review. *J. Raman Spectrosc.* **46**, 4–20 (2015).
- 1158 74. Wang, Y., Huang, W. E., Cui, L. & Wagner, M. Single cell stable isotope probing in microbiology
1159 using Raman microspectroscopy. *Curr. Opin. Biotechnol.* **41**, 34–42 (2016).
- 1160 75. Li, M., Ashok, P. C., Dholakia, K. & Huang, W. E. Raman-activated cell counting for profiling carbon
1161 dioxide fixing microorganisms. *J. Phys. Chem. A* **116**, 6560–6563 (2012).
- 1162 76. Li, M. *et al.* Rapid resonance Raman microspectroscopy to probe carbon dioxide fixation by single
1163 cells in microbial communities. *ISME J.* **6**, 875–885 (2012).
- 1164 77. Li, M., Huang, W. E., Gibson, C. M., Fowler, P. W. & Jousset, A. Stable isotope probing and Raman
1165 spectroscopy for monitoring carbon flow in a food chain and revealing metabolic pathway. *Anal. Chem.*
1166 **85**, 1642–1649 (2013).
- 1167 78. Wang, Y. *et al.* Reverse and multiple stable isotope probing to study bacterial metabolism and
1168 interactions at the single cell level. *Anal. Chem.* **88**, 9443–9450 (2016).
- 1169 79. Cui, L., Butler, H. J., Martin-Hirsch, P. L. & Martin, F. L. Aluminium foil as a potential substrate for
1170 ATR-FTIR, transfection FTIR or Raman spectrochemical analysis of biological specimens. *Anal.*
1171 *Methods* **8**, 481–487 (2016).
- 1172 80. Cui, L., Yang, K., Zhou, G., Huang, W. E. & Zhu, Y.-G. Surface-enhanced Raman spectroscopy
1173 combined with stable isotope probing to monitor nitrogen assimilation at both bulk and single-cell
1174 level. *Anal. Chem.* **89**, 5793–5800 (2017).
- 1175 81. Fernando, E. Y. *et al.* Resolving the individual contribution of key microbial populations to enhanced
1176 biological phosphorus removal with Raman–FISH. *ISME J.* **13**, 1933–1946 (2019).
- 1177 82. Grosser, K. *et al.* Disruption-free imaging by Raman spectroscopy reveals a chemical sphere with
1178 antifouling metabolites around macroalgae. *Biofouling* **28**, 687–696 (2012).
- 1179 83. Gautam, R., Vanga, S., Ariese, F. & Umapathy, S. Review of multidimensional data processing
1180 approaches for Raman and infrared spectroscopy. *EPJ Tech. Instrum.* **2**, 8 (2015).
- 1181 84. Byrne, H. J., Knief, P., Keating, M. E. & Bonnier, F. Spectral pre and post processing for infrared and
1182 Raman spectroscopy of biological tissues and cells. *Chem. Soc. Rev.* **45**, 1865–1878 (2016).
- 1183 85. Savitzky, A.; Golay, M. J. E. Smoothing and differentiation of data by simplified least square
1184 procedures. *Anal. Chem.* **36**, 1627–1639 (1964).
- 1185 86. Schafer, R. W. What is a Savitzky-Golay filter? *IEEE Signal Process. Mag.* **28**, 111–117 (2011).
- 1186 87. Quintero, L., Matthäus, C., Hunt, S. & Diem, M. Denoising of single scan Raman spectroscopy signals.
1187 *Imaging, Manip., Anal., Biomol., Cells, Tissues VIII* **7568**, 756817 (2010).
- 1188 88. Ehrentreich, F. & Sümmchen, L. Spike removal and denoising of Raman spectra by wavelet transform
1189 methods. *Anal. Chem.* **73**, 4364–4373 (2001).
- 1190 89. Ehrentreich, F. Wavelet transform applications in analytical chemistry. *Anal. Bioanal. Chem.* **372**,
1191 115–121 (2002).
- 1192 90. Silveira, L., Bodanese, B., Zangaro, R. A. & Pacheco, M. T. T. Discrete wavelet transform for
1193 denoising Raman spectra of human skin tissues used in a discriminant diagnostic algorithm. *Instrum.*
1194 *Sci. Technol.* **38**, 268–282 (2010).
- 1195 91. Lieber, C. A. & Mahadevan-Jansen, A. Automated method for subtraction of fluorescence from
1196 biological Raman spectra. *Appl. Spectrosc.* **57**, 1363–1367 (2003).
- 1197 92. Zhao, J., Lui, H., McLean, D. I. & Zeng, H. Automated autofluorescence background subtraction
1198 algorithm for biomedical Raman spectroscopy. *Appl. Spectrosc.* **61**, 1225–1232 (2007).
- 1199 93. Eilers, P. H. C. & Boelens, H. F. M. Baseline correction with asymmetric least squares smoothing.
1200 *Leiden Univ. Med. Cent. Rep.* **1**, 1–5 (2005).
- 1201 94. Lasch, P. Spectral pre-processing for biomedical vibrational spectroscopy and microspectroscopic
1202 imaging. *Chemom. Intell. Lab. Syst.* **117**, 100–114 (2012).
- 1203 95. Afseth, N. K., Segtnan, V. H. & Wold, J. P. Raman spectra of biological samples: A study of
1204 preprocessing methods. *Appl. Spectrosc.* **60**, 1358–1367 (2006).
- 1205 96. de Groot, P. J. *et al.* Application of principal component analysis to detect outliers and spectral
1206 deviations in near-field surface-enhanced Raman spectra. *Anal. Chim. Acta* **446**, 71–83 (2001).
- 1207 97. Liu, X.-Y. *et al.* Spatiotemporal organization of biofilm matrix revealed by confocal Raman mapping

- integrated with non-negative matrix factorization analysis. *Anal. Chem.* **92**, 707–715 (2020).
- 1209 98. Schumacher, W., Stöckel, S., Rösch, P. & Popp, J. Improving chemometric results by optimizing the
1210 dimension reduction for Raman spectral data sets. *J. Raman Spectrosc.* **45**, 930–940 (2014).
- 1211 99. Shashilov, V. A., Xu, M., Ermolenkov, V. V. & Lednev, I. K. Latent variable analysis of Raman
1212 spectra for structural characterization of proteins. *J. Quant. Spectrosc. Radiat. Transf.* **102**, 46–61
1213 (2006).
- 1214 100. Lee, T.-W. *Independent Component Analysis – Theory and Applications*. (Springer, New York, 1998).
- 1215 101. Piraino, P., Ricciardi, A., Salzano, G., Zotta, T. & Parente, E. Use of unsupervised and supervised
1216 artificial neural networks for the identification of lactic acid bacteria on the basis of SDS-PAGE
1217 patterns of whole cell proteins. *J. Microbiol. Methods* **66**, 336–346 (2006).
- 1218 102. Schmid, U. *et al.* Gaussian mixture discriminant analysis for the single-cell differentiation of bacteria
1219 using micro-Raman spectroscopy. *Chemom. Intell. Lab. Syst.* **96**, 159–171 (2009).
- 1220 103. Prochazka, D. *et al.* Combination of laser-induced breakdown spectroscopy and Raman spectroscopy
1221 for multivariate classification of bacteria. *Spectrochim. Acta – Part B: At. Spectrosc.* **139**, 6–12 (2018).
- 1222 104. Kloß, S. *et al.* Destruction-free procedure for the isolation of bacteria from sputum samples for Raman
1223 spectroscopic analysis. *Anal. Bioanal. Chem.* **407**, 8333–8341 (2015).
- 1224 105. Hlaing, M. M., Dunn, M., Stoddart, P. R. & McArthur, S. L. Raman spectroscopic identification of
1225 single bacterial cells at different stages of their lifecycle. *Vib. Spectrosc.* **86**, 81–89 (2016).
- 1226 106. Ho, C.-S. *et al.* Rapid identification of pathogenic bacteria using Raman spectroscopy and deep
1227 learning. *Nat. Commun.* **10**, 4927 (2019).
- 1228 107. Živanović, V. *et al.* Optical nanosensing of lipid accumulation due to enzyme inhibition in live cells.
1229 *ACS Nano* **13**, 9363–9375 (2019).
- 1230 108. van de Schoot, R. *et al.* Bayesian statistics and modelling. *Nat. Rev. Methods Prim.* **1**, 1 (2021).
- 1231 109. Rebrošová, K. *et al.* Rapid identification of staphylococci by Raman spectroscopy. *Sci. Rep.* **7**, 14846
1232 (2017).
- 1233 110. Gaus, K. *et al.* Classification of lactic acid bacteria with UV-resonance Raman spectroscopy.
1234 *Biopolymers* **82**, 286–290 (2006).
- 1235 111. Rösch, P. *et al.* Chemotaxonomic identification of single bacteria by micro-Raman spectroscopy:
1236 application to clean-room-relevant biological contaminations. *Appl. Environ. Microbiol.* **71**, 1626–
1237 1637 (2005).
- 1238 112. Errington, J. Regulation of endospore formation in *Bacillus subtilis*. *Nat. Rev. Microbiol.* **1**, 117–126
1239 (2003).
- 1240 113. Huang, S.-S. *et al.* Levels of Ca²⁺-dipicolinic acid in individual *Bacillus* spores determined using
1241 microfluidic Raman tweezers. *J. Bacteriol.* **189**, 4681–4687 (2007).
- 1242 114. Xu, J., Webb, I., Poole, P. & Huang, W. E. Label-free discrimination of rhizobial bacteroids and
1243 mutants by single-cell Raman microspectroscopy. *Anal. Chem.* **89**, 6336–6340 (2017).
- 1244 115. Ng, C. K. *et al.* Elevated intracellular cyclic-di-GMP level in *Shewanella oneidensis* increases
1245 expression of *c*-type cytochromes. *Microb. Biotechnol.* **13**, 1904–1916 (2020).
- 1246 116. Song, Y. *et al.* Single-cell genomics based on Raman sorting reveals novel carotenoid-containing
1247 bacteria in the Red Sea. *Microb. Biotechnol.* **10**, 125–137 (2017).
- 1248 117. Jing, X. *et al.* Raman-activated cell sorting and metagenomic sequencing revealing carbon-fixing
1249 bacteria in the ocean. *Environ. Microbiol.* **20**, 2241–2255 (2018).
- 1250 118. Song, Y. *et al.* Proteorhodopsin overproduction enhances the long-term viability of *Escherichia coli*.
1251 *Appl. Environ. Microbiol.* **86**, e02087-19 (2020).
- 1252 119. Carey, P. R. *Biochemical applications of Raman and resonance Raman spectroscopies*. (Academic
1253 Press, 1982).
- 1254 120. Takano, H. The regulatory mechanism underlying light-inducible production of carotenoids in
1255 nonphototrophic bacteria. *Biosci. Biotechnol. Biochem.* **80**, 1264–1273 (2016).
- 1256 121. Wang, W. *et al.* Structural basis for blue-green light harvesting and energy dissipation in diatoms.
1257 *Science* **363**, eaav0365 (2019).
- 1258 122. Moudříková, Š. *et al.* Raman and fluorescence microscopy sensing energy-transducing and energy-
1259 storing structures in microalgae. *Algal Res.* **16**, 224–232 (2016).
- 1260 123. Yakubovskaya, E., Zaliznyak, T., Martínez Martínez, J. & Taylor, G. T. Tear down the fluorescent

- 1261 curtain: A new fluorescence suppression method for Raman microspectroscopic analyses. *Sci. Rep.* **9**,
1262 15785 (2019).
- 1263 124. Vogt, C. *et al.* Stable isotope probing approaches to study anaerobic hydrocarbon degradation and
1264 degraders. *J. Mol. Microbiol. Biotechnol.* **26**, 195–210 (2016).
- 1265 125. van Manen, H.-J., Lenferink, A. & Otto, C. Noninvasive imaging of protein metabolic labeling in
1266 single human cells using stable isotopes and Raman microscopy. *Anal. Chem.* **80**, 9576–9582 (2008).
- 1267 126. Xu, J. *et al.* Raman deuterium isotope probing reveals microbial metabolism at the single-cell level.
1268 *Anal. Chem.* **89**, 13305–13312 (2017).
- 1269 127. Olaniyi, O. O., Yang, K., Zhu, Y.-G. & Cui, L. Heavy water-labeled Raman spectroscopy reveals
1270 carboxymethylcellulose-degrading bacteria and degradation activity at the single-cell level. *Appl.*
1271 *Microbiol. Biotechnol.* **103**, 1455–1464 (2019).
- 1272 128. Huang, W. E. *et al.* Resolving genetic functions within microbial populations: In situ analyses using
1273 rRNA and mRNA stable isotope probing coupled with single-cell Raman-fluorescence in situ
1274 hybridization. *Appl. Environ. Microbiol.* **75**, 234–241 (2009).
- 1275 129. Singleton, C. M. *et al.* Connecting structure to function with the recovery of over 1000 high-quality
1276 metagenome-assembled genomes from activated sludge using long-read sequencing. *Nat. Commun.* **12**,
1277 2009 (2021).
- 1278 130. Milucka, J. *et al.* Zero-valent sulphur is a key intermediate in marine methane oxidation. *Nature* **491**,
1279 541–546 (2012).
- 1280 131. Schmid, T., Messmer, A., Yeo, B.-S., Zhang, W. & Zenobi, R. Towards chemical analysis of
1281 nanostructures in biofilms II: Tip-enhanced Raman spectroscopy of alginates. *Anal. Bioanal. Chem.*
1282 **391**, 1907–1916 (2008).
- 1283 132. Madzharova, F., Heiner, Z., Gühlke, M. & Kneipp, J. Surface-enhanced hyper-Raman spectra of
1284 adenine, guanine, cytosine, thymine, and uracil. *J. Phys. Chem. C* **120**, 15415–15423 (2016).
- 1285 133. Kim, S. K., Joo, T. H., Suh, S. W. & Kim, M. S. Surface-enhanced Raman scattering (SERS) of
1286 nucleic acid components in silver sol: Adenine series. *J. Raman Spectrosc.* **17**, 381–386 (1986).
- 1287 134. Feng, F. *et al.* SERS detection of low-concentration adenine by a patterned silver structure immersion
1288 plated on a silicon nanoporous pillar array. *Nanotechnology* **20**, 295501 (2009).
- 1289 135. Bell, S. E. J. *et al.* Towards reliable and quantitative surface-enhanced Raman scattering (SERS): From
1290 key parameters to good analytical practice. *Angew. Chem. Int. Ed.* **59**, 5454–5462 (2020).
- 1291 136. Zhang, M. *et al.* Rapid determination of antimicrobial susceptibility by stimulated Raman scattering
1292 imaging of D₂O metabolic incorporation in a single bacterium. *Adv. Sci.* **7**, 2001452 (2020).
- 1293 137. Karanja, C. W. *et al.* Stimulated Raman imaging reveals aberrant lipogenesis as a metabolic marker for
1294 azole-resistant *Candida albicans*. *Anal. Chem.* **89**, 9822–9829 (2017).
- 1295 138. Majed, N., Chernenko, T., Diem, M. & Gu, A. Z. Identification of functionally relevant populations in
1296 enhanced biological phosphorus removal processes based on intracellular polymers profiles and
1297 insights into the metabolic diversity and heterogeneity. *Environ. Sci. Technol.* **46**, 5010–5017 (2012).
- 1298 139. Li, Y. *et al.* Toward better understanding of EBPR systems via linking Raman-based phenotypic
1299 profiling with phylogenetic diversity. *Environ. Sci. Technol.* **52**, 8596–8606 (2018).
- 1300 140. Spang, A. *et al.* The genome of the ammonia-oxidizing *Candidatus Nitrososphaera gargensis*: insights
1301 into metabolic versatility and environmental adaptations. *Environ. Microbiol.* **14**, 3122–3145 (2012).
- 1302 141. Probst, A. J. *et al.* Biology of a widespread uncultivated archaeon that contributes to carbon fixation in
1303 the subsurface. *Nat. Commun.* **5**, 5497 (2014).
- 1304 142. Hong, W. *et al.* In situ detection of a single bacterium in complex environment by hyperspectral CARS
1305 imaging. *ChemistrySelect* **1**, 513–517 (2016).
- 1306 143. Petrov, G. I. *et al.* Comparison of coherent and spontaneous Raman microspectroscopies for
1307 noninvasive detection of single bacterial endospores. *Proc. Natl. Acad. Sci. U. S. A.* **104**, 7776–7779
1308 (2007).
- 1309 144. Arora, R., Petrov, G. I., Yakovlev, V. V. & Scully, M. O. Detecting anthrax in the mail by coherent
1310 Raman microspectroscopy. *Proc. Natl. Acad. Sci. U. S. A.* **109**, 1151–1153 (2012).
- 1311 145. Hong, W. *et al.* Antibiotic susceptibility determination within one cell cycle at single-bacterium level
1312 by stimulated Raman metabolic imaging. *Anal. Chem.* **90**, 3737–3743 (2018).
- 1313 146. He, Y., Wang, X., Ma, B. & Xu, J. Ramanome technology platform for label-free screening and sorting

- 1314 of microbial cell factories at single-cell resolution. *Biotechnol. Adv.* **37**, 107388 (2019).
- 1315 147. Kjeldsen, K. U. *et al.* On the evolution and physiology of cable bacteria. *Proc. Natl. Acad. Sci. U. S. A.*
- 1316 **116**, 19116–19125 (2019).
- 1317 148. Bjerg, J. T. *et al.* Long-distance electron transport in individual, living cable bacteria. *Proc. Natl. Acad.*
- 1318 *Sci. U. S. A.* **115**, 5786–5791 (2018).
- 1319 149. Haider, S. *et al.* Raman microspectroscopy reveals long-term extracellular activity of chlamydiae. *Mol.*
- 1320 *Microbiol.* **77**, 687–700 (2010).
- 1321 150. Chen, D., Huang, S.-S. & Li, Y.-Q. Real-time detection of kinetic germination and heterogeneity of
- 1322 single *Bacillus* spores by laser tweezers Raman spectroscopy. *Anal. Chem.* **78**, 6936–6941 (2006).
- 1323 151. Jäckle, O. *et al.* Chemosynthetic symbiont with a drastically reduced genome serves as primary energy
- 1324 storage in the marine flatworm *Paracatenula*. *Proc. Natl. Acad. Sci. U. S. A.* **116**, 8505–8514 (2019).
- 1325 152. Sharma, K., Palatinszky, M., Nikolov, G., Berry, D. & Shank, E. A. Transparent soil microcosms for
- 1326 live-cell imaging and non-destructive stable isotope probing of soil microorganisms. *Elife* **9**, e56275
- 1327 (2020).
- 1328 153. Bodelón, G. *et al.* Detection and imaging of quorum sensing in *Pseudomonas aeruginosa* biofilm
- 1329 communities by surface-enhanced resonance Raman scattering. *Nat. Mater.* **15**, 1203–1211 (2016).
- 1330 154. Sandt, C., Smith-Palmer, T., Pink, J., Brennan, L. & Pink, D. Confocal Raman microspectroscopy as a
- 1331 tool for studying the chemical heterogeneities of biofilms in situ. *J. Appl. Microbiol.* **103**, 1808–1820
- 1332 (2007).
- 1333 155. Ivleva, N. P. *et al.* Label-free in situ SERS imaging of biofilms. *J. Phys. Chem. B* **114**, 10184–10194
- 1334 (2010).
- 1335 156. Ivleva, N. P., Wagner, M., Horn, H., Niessner, R. & Haisch, C. Towards a nondestructive chemical
- 1336 characterization of biofilm matrix by Raman microscopy. *Anal. Bioanal. Chem.* **393**, 197–206 (2009).
- 1337 157. Horiue, H., Sasaki, M., Yoshikawa, Y., Toyofuku, M. & Shigeto, S. Raman spectroscopic signatures of
- 1338 carotenoids and polyenes enable label-free visualization of microbial distributions within pink biofilms.
- 1339 *Sci. Rep.* **10**, 7704 (2020).
- 1340 158. Schiessl, K. T. *et al.* Phenazine production promotes antibiotic tolerance and metabolic heterogeneity
- 1341 in *Pseudomonas aeruginosa* biofilms. *Nat. Commun.* **10**, 762 (2019).
- 1342 159. Singer, E., Wagner, M. & Woyke, T. Capturing the genetic makeup of the active microbiome *in situ*.
- 1343 *ISME J.* **11**, 1949–1963 (2017).
- 1344 160. Hong, J.-K., Kim, S. B., Lyoo, E. S. & Lee, T. K. Microbial phenomics linking the phenotype to
- 1345 function: The potential of Raman spectroscopy. *J. Microbiol.* **59**, 249–258 (2021).
- 1346 161. Hatzenpichler, R., Krukenberg, V., Spietz, R. L. & Jay, Z. J. Next-generation physiology approaches to
- 1347 study microbiome function at single cell level. *Nat. Rev. Microbiol.* **18**, 241–256 (2020).
- 1348 162. Jing, X. *et al.* One-cell metabolic phenotyping and sequencing of soil microbiome by Raman-activated
- 1349 gravity-driven encapsulation (RAGE). *mSystems* **6**, e00181-21 (2021).
- 1350 163. Kim, H. S. *et al.* Raman spectroscopy compatible PDMS droplet microfluidic culture and analysis
- 1351 platform towards on-chip lipidomics. *Analyst* **142**, 1054–1060 (2017).
- 1352 164. Wang, X. *et al.* Raman-activated droplet sorting (RADS) for label-free high-throughput screening of
- 1353 microalgal single-cells. *Anal. Chem.* **89**, 12569–12577 (2017).
- 1354 165. Lorenz, B., Wichmann, C., Stöckel, S., Rösch, P. & Popp, J. Cultivation-free Raman spectroscopic
- 1355 investigations of bacteria. *Trends Microbiol.* **25**, 413–424 (2017).
- 1356 166. Rösch, P. *et al.* Online monitoring and identification of bioaerosols. *Anal. Chem.* **78**, 2163–2170
- 1357 (2006).
- 1358 167. Locke, A., Fitzgerald, S. & Mahadevan-Jansen, A. Advances in optical detection of human-associated
- 1359 pathogenic bacteria. *Molecules* **25**, 5256 (2020).
- 1360 168. Maruthamuthu, M. K., Raffiee, A. H., De Oliveira, D. M., Ardekani, A. M. & Verma, M. S. Raman
- 1361 spectra-based deep learning: A tool to identify microbial contamination. *Microbiologypopen* **9**, e1122
- 1362 (2020).
- 1363 169. de Siqueira e Oliveira, F. S. A., da Silva, A. M., Pacheco, M. T. T., Giana, H. E. & Silveira, L.
- 1364 Biochemical characterization of pathogenic bacterial species using Raman spectroscopy and
- 1365 discrimination model based on selected spectral features. *Lasers Med. Sci.* **36**, 289–302 (2021).
- 1366 170. Wang, K. *et al.* *Arcobacter* identification and species determination using Raman spectroscopy

- 1367 combined with neural networks. *Appl. Environ. Microbiol.* **86**, e00924-20 (2020).
- 1368 171. Yu, S., Li, H., Li, X., Fu, Y. V. & Liu, F. Classification of pathogens by Raman spectroscopy
1369 combined with generative adversarial networks. *Sci. Total Environ.* **726**, 138477 (2020).
- 1370 172. Lorenz, B., Ali, N., Bocklitz, T., Rösch, P. & Popp, J. Discrimination between pathogenic and non-
1371 pathogenic *E. coli* strains by means of Raman microspectroscopy. *Anal. Bioanal. Chem.* **412**, 8241–
1372 8247 (2020).
- 1373 173. Verma, T., Annappa, H., Singh, S., Umopathy, S. & Nandi, D. Profiling antibiotic resistance in
1374 *Escherichia coli* strains displaying differential antibiotic susceptibilities using Raman spectroscopy. *J.*
1375 *Biophotonics* **14**, e202000231 (2021).
- 1376 174. Götz, T. *et al.* Automated and rapid identification of multidrug resistant *Escherichia coli* against the
1377 lead drugs of acylureidopenicillins, cephalosporins, and fluoroquinolones using specific Raman marker
1378 bands. *J. Biophotonics* **13**, e202000149 (2020).
- 1379 175. Kriem, L. S., Wright, K., Ccahuana-Vasquez, R. A. & Rupp, S. Confocal Raman microscopy to
1380 identify bacteria in oral subgingival biofilm models. *PLoS One* **15**, e0232912 (2020).
- 1381 176. Kochan, K. *et al.* Vibrational spectroscopy as a sensitive probe for the chemistry of intra-phase
1382 bacterial growth. *Sensors* **20**, 3452 (2020).
- 1383 177. Stöckel, S., Kirchhoff, J., Neugebauer, U., Rösch, P. & Popp, J. The application of Raman
1384 spectroscopy for the detection and identification of microorganisms. *J. Raman Spectrosc.* **47**, 89–109
1385 (2016).
- 1386 178. Pahlow, S. *et al.* Isolation and identification of bacteria by means of Raman spectroscopy. *Adv. Drug*
1387 *Deliv. Rev.* **89**, 105–120 (2015).
- 1388 179. Qian, X. *et al.* *In vivo* tumor targeting and spectroscopic detection with surface-enhanced Raman
1389 nanoparticle tags. *Nat. Biotechnol.* **26**, 83–90 (2008).
- 1390 180. Porter, M. D., Lipert, R. J., Siperko, L. M., Wang, G. & Narayanan, R. SERS as a bioassay platform:
1391 fundamentals, design, and applications. *Chem. Soc. Rev.* **37**, 1001–1011 (2008).
- 1392 181. Yakes, B. J., Lipert, R. J., Bannantine, J. P. & Porter, M. D. Detection of *Mycobacterium avium* subsp.
1393 *paratuberculosis* by a sonicate immunoassay based on surface-enhanced Raman scattering. *Clin.*
1394 *Vaccine Immunol.* **15**, 227–234 (2008).
- 1395 182. Wang, C., Madiyar, F., Yu, C. & Li, J. Detection of extremely low concentration waterborne pathogen
1396 using a multiplexing self-referencing SERS microfluidic biosensor. *J. Biol. Eng.* **11**, 9 (2017).
- 1397 183. Catala, C. *et al.* Online SERS quantification of *Staphylococcus aureus* and the application to
1398 diagnostics in human fluids. *Adv. Mater. Technol.* **1**, 1600163 (2016).
- 1399 184. Pazos-Perez, N. *et al.* Ultrasensitive multiplex optical quantification of bacteria in large samples of
1400 biofluids. *Sci. Rep.* **6**, 29014 (2016).
- 1401 185. Shi, L. *et al.* Rapid, quantitative, high-sensitive detection of *Escherichia coli* O157:H7 by gold-shell
1402 silica-core nanospheres-based surface-enhanced Raman scattering lateral flow immunoassay. *Front.*
1403 *Microbiol.* **11**, 596005 (2020).
- 1404 186. You, S.-M. *et al.* Gold nanoparticle-coated starch magnetic beads for the separation, concentration, and
1405 SERS-based detection of *E. coli* O157:H7. *ACS Appl. Mater. Interfaces* **12**, 18292–18300 (2020).
- 1406 187. Hong, W.-E. *et al.* Assembled growth of 3D Fe₃O₄@Au nanoparticles for efficient photothermal
1407 ablation and SERS detection of microorganisms. *J. Mater. Chem. B* **6**, 5689–5697 (2018).
- 1408 188. Opota, O., Croxatto, A., Prod'homme, G. & Greub, G. Blood culture-based diagnosis of bacteraemia:
1409 state of the art. *Clin. Microbiol. Infect.* **21**, 313–322 (2015).
- 1410 189. Cross, K. L. *et al.* Targeted isolation and cultivation of uncultivated bacteria by reverse genomics. *Nat.*
1411 *Biotechnol.* **37**, 1314–1321 (2019).
- 1412 190. Samek, O. *et al.* Quantitative Raman spectroscopy analysis of polyhydroxyalkanoates produced by
1413 *Cupriavidus necator* H16. *Sensors* **16**, 1808 (2016).
- 1414 191. Berg, J. S., Schwedt, A., Kreutzmann, A.-C., Kuypers, M. M. M. & Milucka, J. Polysulfides as
1415 intermediates in the oxidation of sulfide to sulfate by *Beggiatoa* spp. *Appl. Environ. Microbiol.* **80**,
1416 629–636 (2014).
- 1417 192. Taylor, G. T. Windows into microbial seascapes: advances in nanoscale imaging and application to
1418 marine sciences. *Ann. Rev. Mar. Sci.* **11**, 465–490 (2019).
- 1419 193. Cohen, A. B. *et al.* Applying fluorescence in situ hybridization to aquatic systems with cyanobacteria

- blooms: Autofluorescence suppression and high-throughput image analysis. *Limnol. Oceanogr. Methods* **19**, 457–475 (2021).
194. Zeller, P., Ploux, O. & Méjean, A. A simple protocol for attenuating the auto-fluorescence of cyanobacteria for optimized fluorescence in situ hybridization (FISH) imaging. *J. Microbiol. Methods* **122**, 16–19 (2016).
195. Woyke, T. *et al.* Assembling the marine metagenome, one cell at a time. *PLoS One* **4**, e5299 (2009).
196. Ben-Amor, K. *et al.* Genetic diversity of viable, injured, and dead fecal bacteria assessed by fluorescence-activated cell sorting and 16S rRNA gene analysis. *Appl. Environ. Microbiol.* **71**, 4679–4689 (2005).
197. Hatzenpichler, R. *et al.* Visualizing in situ translational activity for identifying and sorting slow-growing archaeal - bacterial consortia. *Proc. Natl. Acad. Sci. U. S. A.* **113**, E4069–E4078 (2016).
198. Grieb, A. *et al.* A pipeline for targeted metagenomics of environmental bacteria. *Microbiome* **8**, 21 (2020).
199. Gong, L., Zheng, W., Ma, Y. & Huang, Z. Higher-order coherent anti-Stokes Raman scattering microscopy realizes label-free super-resolution vibrational imaging. *Nat. Photonics* **14**, 115–122 (2020).
200. Xiong, H. *et al.* Super-resolution vibrational microscopy by stimulated Raman excited fluorescence. *Light Sci. Appl.* **10**, 87 (2021).
201. Watanabe, K. *et al.* Structured line illumination Raman microscopy. *Nat. Commun.* **6**, 10095 (2015).
202. Kögler, M., Itkonen, J., Viitala, T. & Casteleijn, M. G. Assessment of recombinant protein production in *E. coli* with Time-Gated Surface Enhanced Raman Spectroscopy (TG-SERS). *Sci. Rep.* **10**, 2472 (2020).
203. Kögler, M. *et al.* Comparison of time-gated surface-enhanced Raman spectroscopy (TG-SERS) and classical SERS based monitoring of *Escherichia coli* cultivation samples. *Biotechnol. Prog.* **34**, 1533–1542 (2018).
204. Shkolyar, S. *et al.* Detecting kerogen as a biosignature using colocated UV time-gated Raman and fluorescence spectroscopy. *Astrobiology* **18**, 431–453 (2018).
205. Yu, S., Piao, X. & Park, N. Machine learning identifies scale-free properties in disordered materials. *Nat. Commun.* **11**, 4842 (2020).
206. Zhong, M., Girolami, M., Faulds, K. & Graham, D. Bayesian methods to detect dye-labelled DNA oligonucleotides in multiplexed Raman spectra. *J. R. Stat. Soc. Ser. C Appl. Stat.* **60**, 187–206 (2011).
207. Astle, W., De Iorio, M., Richardson, S., Stephens, D. & Ebbels, T. A Bayesian model of NMR spectra for the deconvolution and quantification of metabolites in complex biological mixtures. *J. Am. Stat. Assoc.* **107**, 1259–1271 (2012).
208. Han, N. & Ram, R. J. Bayesian modeling and computation for analyte quantification in complex mixtures using Raman spectroscopy. *Comput. Stat. Data Anal.* **143**, 106846 (2020).
209. Rubtsov, D. V. *et al.* Application of a Bayesian deconvolution approach for high-resolution ¹H NMR spectra to assessing the metabolic effects of acute phenobarbital exposure in liver tissue. *Anal. Chem.* **82**, 4479–4485 (2010).
210. Weljie, A. M., Newton, J., Mercier, P., Carlson, E. & Slupsky, C. M. Targeted profiling: quantitative analysis of 1H NMR metabolomics data. *Anal. Chem.* **78**, 4430–4442 (2006).
211. Hao, J., Astle, W., De Iorio, M. & Ebbels, T. M. D. Batman-an R package for the automated quantification of metabolites from nuclear magnetic resonance spectra using a Bayesian model. *Bioinformatics* **28**, 2088–2090 (2012).
212. Goodacre, R. Explanatory analysis of spectroscopic data using machine learning of simple, interpretable rules. *Vib. Spectrosc.* **32**, 33–45 (2003).
213. Goodacre, R. *et al.* Rapid identification of urinary tract infection bacteria using hyperspectral whole-organism fingerprinting and artificial neural networks. *Microbiology* **144**, 1157–1170 (1998).
214. Nims, C., Cron, B., Wetherington, M., Macalady, J. & Cosmidis, J. Low frequency Raman Spectroscopy for micron-scale and in vivo characterization of elemental sulfur in microbial samples. *Sci. Rep.* **9**, 7971 (2019).
215. Eder, S. H. K., Gigler, A. M., Hanzlik, M. & Winkhofer, M. Sub-micrometer-scale mapping of magnetite crystals and sulfur globules in magnetotactic bacteria using confocal Raman micro-

- 1473 spectrometry. *PLoS One* **9**, e107356 (2014).
- 1474 216. Zhu, T.-T., Tian, L.-J., Yu, S.-S. & Yu, H.-Q. Roles of cation efflux pump in biomineralization of
1475 cadmium into quantum dots in *Escherichia coli*. *J. Hazard. Mater.* **412**, 125248 (2021).
- 1476 217. Choy, C. A. *et al.* The vertical distribution and biological transport of marine microplastics across the
1477 epipelagic and mesopelagic water column. *Sci. Rep.* **9**, 7843 (2019).
- 1478 218. Jiang, P., Zhao, S., Zhu, L. & Li, D. Microplastic-associated bacterial assemblages in the intertidal
1479 zone of the Yangtze Estuary. *Sci. Total Environ.* **624**, 48–54 (2018).
- 1480 219. Frère, L. *et al.* Microplastic bacterial communities in the Bay of Brest: Influence of polymer type and
1481 size. *Environ. Pollut.* **242**, 614–625 (2018).
- 1482 220. Brewer, P. G. *et al.* Development of a laser Raman spectrometer for deep-ocean science. *Deep-Sea Res.*
1483 *Pt. I* **51**, 739–753 (2004).
- 1484 221. White, S. N. Laser Raman spectroscopy as a technique for identification of seafloor hydrothermal and
1485 cold seep minerals. *Chem. Geol.* **259**, 240–252 (2009).
- 1486 222. Rull, F. *et al.* The Raman laser spectrometer for the ExoMars Rover Mission to Mars. *Astrobiology* **17**,
1487 627–654 (2017).
- 1488 223. Scanning Habitable Environments with Raman & Luminescence for Organics & Chemicals
1489 (SHERLOC) - NASA Mars. <https://mars.nasa.gov/mars2020/spacecraft/instruments/sherloc/>.
- 1490 224. Veneranda, M. *et al.* ExoMars Raman Laser Spectrometer (RLS): development of chemometric tools
1491 to classify ultramafic igneous rocks on Mars. *Sci. Rep.* **10**, 16954 (2020).
- 1492 225. Veneranda, M. *et al.* ExoMars Raman laser spectrometer: A tool for the potential recognition of wet-
1493 target craters on Mars. *Astrobiology* **20**, 349–363 (2020).
- 1494 226. Messmer, M. W., Dieser, M., Smith, H. J., Parker, A. E. & Foreman, C. M. Investigation of Raman
1495 spectroscopic signatures with multivariate statistics: An approach for cataloguing microbial
1496 biosignatures. *Astrobiology* **22**, 1–11 (2022).
- 1497 227. Arnold, F. H. & Georgiou, G. *Directed Enzyme Evolution: Screening and Selection Methods*. (Humana
1498 Press, 2003).
- 1499 228. Markel, U. *et al.* Advances in ultrahigh-throughput screening for directed enzyme evolution. *Chem.*
1500 *Soc. Rev.* **49**, 233–262 (2020).
- 1501 229. Peng, L. *et al.* Intracellular ethanol accumulation in yeast cells during aerobic fermentation: A Raman
1502 spectroscopic exploration. *Lett. Appl. Microbiol.* **51**, 632–638 (2010).
- 1503 230. Cecchini, M. P. *et al.* Ultrafast surface enhanced resonance Raman scattering detection in droplet-
1504 based microfluidic systems. *Anal. Chem.* **83**, 3076–3081 (2011).
- 1505 231. März, A., Henkel, T., Cialla, D., Schmitt, M. & Popp, J. Droplet formation via flow-through
1506 microdevices in Raman and surface enhanced Raman spectroscopy - concepts and applications. *Lab*
1507 *Chip* **11**, 3584–3592 (2011).
- 1508 232. Moore, B. D. *et al.* Rapid and ultra-sensitive determination of enzyme activities using surface-
1509 enhanced resonance Raman scattering. *Nat. Biotechnol.* **22**, 1133–1138 (2004).
- 1510 233. Hutter, E. & Fendler, J. H. Exploitation of localized surface plasmon resonance. *Adv. Mater.* **16**, 1685–
1511 1706 (2004).
- 1512 234. Pilot, R. *et al.* A review on surface-enhanced Raman scattering. *Biosensors* **9**, 57 (2019).
- 1513 235. Cui, L., Zhang, D. D., Yang, K., Zhang, X. & Zhu, Y.-G. Perspective on surface-enhanced Raman
1514 spectroscopic investigation of microbial world. *Anal. Chem.* **91**, 15345–15354 (2019).
- 1515 236. Sharma, B., Frontiera, R. R., Henry, A.-I., Ringe, E. & Van Duyne, R. P. SERS: Materials,
1516 applications, and the future. *Mater. Today* **15**, 16–25 (2012).
- 1517 237. Madzharova, F., Heiner, Z., Simke, J., Selve, S. & Kneipp, J. Gold nanostructures for plasmonic
1518 enhancement of hyper-Raman scattering. *J. Phys. Chem. C* **122**, 2931–2940 (2018).
- 1519 238. Wagner, M. & Haider, S. New trends in fluorescence *in situ* hybridization for identification and
1520 functional analyses of microbes. *Curr. Opin. Biotechnol.* **23**, 96–102 (2012).
- 1521 239. Daims, H., Lückner, S. & Wagner, M. Daimo, a novel image analysis program for microbial ecology
1522 and biofilm research. *Environ. Microbiol.* **8**, 200–213 (2006).
- 1523 240. Hoshino, T., Yilmaz, L. S., Noguera, D. R., Daims, H. & Wagner, M. Quantification of target
1524 molecules needed to detect microorganisms by fluorescence *in situ* hybridization (FISH) and catalyzed
1525 reporter deposition-FISH. *Appl. Environ. Microbiol.* **74**, 5068–5077 (2008).

- 1526 241. Amann, R., Snaidr, J., Wagner, M., Ludwig, W. & Schleifer, K. H. In situ visualization of high genetic
1527 diversity in a natural microbial community. *J. Bacteriol.* **178**, 3496–3500 (1996).
- 1528 242. Lukumbuzya, M., Schmid, M., Pjevac, P. & Daims, H. A multicolor fluorescence *in situ* hybridization
1529 approach using an extended set of fluorophores to visualize microorganisms. *Front. Microbiol.* **10**,
1530 1383 (2019).
- 1531 243. Valm, A. M. *et al.* Systems-level analysis of microbial community organization through combinatorial
1532 labeling and spectral imaging. *Proc. Natl. Acad. Sci. U. S. A.* **108**, 4152–4157 (2011).
- 1533 244. Heldal, M., Norland, S. & Tুমyr, O. X-ray microanalytic method for measurement of dry matter and
1534 elemental content of individual bacteria. *Appl. Environ. Microbiol.* **50**, 1251–1257 (1985).
- 1535 245. Wei, L., Yu, Y., Shen, Y., Wang, M. C. & Min, W. Vibrational imaging of newly synthesized proteins
1536 in live cells by stimulated Raman scattering microscopy. *Proc. Natl. Acad. Sci. U. S. A.* **110**, 11226–
1537 11231 (2013).
- 1538 246. Li, J. & Cheng, J.-X. Direct visualization of de novo lipogenesis in single living cells. *Sci. Rep.* **4**, 6807
1539 (2014).
- 1540 247. Gao, C. *et al.* Single-cell bacterial transcription measurements reveal the importance of
1541 dimethylsulfoniopropionate (DMSP) hotspots in ocean sulfur cycling. *Nat. Commun.* **11**, 1942 (2020).
- 1542 248. Kopf, S. H. *et al.* Heavy water and ¹⁵N labelling with NanoSIMS analysis reveals growth rate-
1543 dependent metabolic heterogeneity in chemostats. *Environ. Microbiol.* **17**, 2542–2556 (2015).
- 1544 249. Crespi, H. L., Conrad, S. M., Uphaus, R. A. & Katz, J. J. Cultivation of microorganisms in heavy water.
1545 *Ann. N. Y. Acad. Sci.* **84**, 648–666 (1960).
- 1546 250. Kseliková, V., Vítová, M. & Bišová, K. Deuterium and its impact on living organisms. *Folia Microbiol.*
1547 (*Praha*). **64**, 673–681 (2019).
- 1548 251. Matanfack, G. A., Pistiki, A., Rösch, P. & Popp, J. Raman ¹⁸O-labeling of bacteria in visible and deep
1549 UV-ranges. *J. Biophotonics* **14**, e202100013 (2021).
- 1550 252. Yan, S. *et al.* Development overview of Raman-activated cell sorting devoted to bacterial detection at
1551 single-cell level. *Appl. Microbiol. Biotechnol.* **105**, 1315–1331 (2021).
- 1552 253. Wang, Y. *et al.* Raman activated cell ejection for isolation of single cells. *Anal. Chem.* **85**, 10697–
1553 10701 (2013).
- 1554 254. Sidore, A. M., Lan, F., Lim, S. W. & Abate, A. R. Enhanced sequencing coverage with digital droplet
1555 multiple displacement amplification. *Nucleic Acids Res.* **44**, e66 (2016).
- 1556
1557
- 1558 35. Drescher, D., Traub, H., Büchner, T., Jakubowski, N. & Kneipp, J. Properties of *in situ* generated gold
1559 nanoparticles in the cellular context. *Nanoscale* **9**, 11647–11656 (2017).
- 1560 **Demonstration of the fabrication of SERS substrates in cellular environment *in situ*.**
- 1561
- 1562 43. Kneipp, J., Kneipp, H. & Kneipp, K. Two-photon vibrational spectroscopy for biosciences based on
1563 surface-enhanced hyper-Raman scattering. *Proc. Natl. Acad. Sci. U. S. A.* **103**, 17149–17153 (2006).
- 1564 **Application of hyper Raman spectroscopy for the detection of complementary peaks of biomolecules**
1565 **and cells.**
- 1566
- 1567 50. Suzuki, Y. *et al.* Label-free chemical imaging flow cytometry by high-speed multicolor stimulated Raman
1568 scattering. *Proc. Natl. Acad. Sci. U. S. A.* **116**, 15842–15848 (2019).
- 1569 **Development of a high-throughput Raman-based flow cell counter for microalgae based on multicolor-**
1570 **stimulated Raman scattering (SRS) microscopy and deep learning.**
- 1571
- 1572 62. Huang, W. E. *et al.* Raman-FISH: Combining stable-isotope Raman spectroscopy and fluorescence *in situ*
1573 hybridization for the single cell analysis of identity and function. *Environ. Microbiol.* **9**, 1878–1889 (2007).
- 1574 **First demonstration of the combination of fluorescence *in situ* hybridization (FISH), stable isotope**
1575 **probing and Raman microspectroscopy.**
- 1576
- 1577 63. Lee, K. S. *et al.* An automated Raman-based platform for the sorting of live cells by functional properties.
1578 *Nat. Microbiol.* **4**, 1035–1048 (2019).

1579 **Sorting of microbial cells in terms of their functional properties (phenotypes) using confocal Raman**
1580 **microspectroscopy, optical tweezers, stable isotope probing, and microfluidics, which enables linking of**
1581 **cell function to their genome through downstream DNA analysis, as well as cultivation for further**
1582 **ecological evaluation.**

1583

1584 68. Taylor, G. T. *et al.* Single-cell growth rates in photoautotrophic populations measured by stable isotope
1585 probing and resonance Raman microspectrometry. *Front. Microbiol.* **8**, 1449 (2017).
1586 **Growth rate measurements of photoautotrophic microbes (*Synechococcus* sp. and *Thalassiosira***
1587 ***pseudonana*) by coupling ¹³C stable isotope probing and single-cell resonance Raman microspectroscopy.**
1588

1589 69. Pereira, F.C. *et al.* Rational design of a microbial consortium of mucosal sugar utilizers reduces
1590 *Clostridiodes difficile* colonization. *Nat. Commun.* **11**, 5104 (2020).
1591 **Application of a high-throughput optofluidic Raman-activated cell sorting (RACS) platform and mini-**
1592 **metagenomics to identify mucosal sugar degraders within gut microbiota and uses this information to**
1593 **rationally design a probiotic mixture of microorganisms that could reduce pathogen colonization.**
1594

1595 70. Berry, D. *et al.* Tracking heavy water (D₂O) incorporation for identifying and sorting active microbial
1596 cells. *Proc. Natl Acad. Sci. USA* **112**, E194–E203 (2015).
1597 **First study combining deuterium labelling, Raman-activated cell sorting and 16S rRNA gene**
1598 **sequencing, which together led to the identification of novel glucosamine- and mucin-utilizing bacteria**
1599 **from mouse gut microbiota.**
1600

1601 81. Fernando, E. Y. *et al.* Resolving the individual contribution of key microbial populations to enhanced
1602 biological phosphorus removal with Raman–FISH. *ISME J.* **13**, 1933–1946 (2019).
1603 **Application of FISH–Raman to quantify the amount of polyphosphate in various microbial taxa in**
1604 **wastewater treatment plants — showing that *Tetrasphaera* play a more important role in enhanced**
1605 **biological phosphorous removal than previously thought.**
1606

1607 106. Ho, C.-S. *et al.* Rapid identification of pathogenic bacteria using Raman spectroscopy and deep learning.
1608 *Nat. Commun.* **10**, 4927 (2019).
1609 **Application of Raman spectroscopy and deep learning to identify 30 common bacterial pathogens with**
1610 **high accuracy (up to 97%).**
1611

1612 111. Rösch, P. *et al.* Chemotaxonomic identification of single bacteria by micro-Raman spectroscopy:
1613 application to clean-room-relevant biological contaminations. *Appl. Environ. Microbiol.* **71**, 1626–1637
1614 (2005).
1615 **First study identifying single bacteria without cultivation using Raman spectroscopy.**
1616

1617 136. Zhang, M. *et al.* Rapid determination of antimicrobial susceptibility by stimulated Raman scattering
1618 imaging of D₂O metabolic incorporation in a single bacterium. *Adv. Sci.* **7**, 2001452 (2020).
1619 **Rapid antimicrobial susceptibility testing based on femtosecond stimulated Raman scattering (SRS)**
1620 **imaging of deuterium incorporation into cells of interest.**
1621

1622 148. Bjerg, J. T. *et al.* Long-distance electron transport in individual, living cable bacteria. *Proc. Natl. Acad.*
1623 *Sci. U. S. A.* **115**, 5786–5791 (2018).
1624 **Resonance Raman measurements of cytochrome demonstrated long-distance electron transport over**
1625 **micrometers in cable bacteria.**
1626

1627 149. Haider, S. *et al.* Raman microspectroscopy reveals long-term extracellular activity of chlamydiae. *Mol.*
1628 *Microbiol.* **77**, 687–700 (2010).
1629 **By using Raman microspectroscopy to differentiate developmental stages of chlamydiae and to**
1630 **investigate the physiological activity of these stages by single cell stable isotope probing it could be**
1631 **demonstrated that in contrast to textbook knowledge elementary bodies of chlamydia are**

1632 **physiologically active outside of their host cells - a feature that has important implications for our**
1633 **understanding of the biology of these pathogens.**
1634
1635 153. Bodelón, G. *et al.* Detection and imaging of quorum sensing in *Pseudomonas aeruginosa* biofilm
1636 communities by surface-enhanced resonance Raman scattering. *Nat. Mater.* **15**, 1203–1211 (2016).
1637 ***In situ*, label-free identification of the structure of growing biofilms, and of their metabolites involved in**
1638 **intercellular signaling (quorum sensing).**
1639
1640 201. Watanabe, K. *et al.* Structured line illumination Raman microscopy. *Nat. Commun.* **6**, 10095 (2015).
1641 **Super-resolution Raman microscopy — structured line illumination to increase the spatial resolution**
1642 **below the Rayleigh limit.**
1643

1644 **Acknowledgements**

1645 R.S. acknowledges support from a Gordon and Betty Moore Foundation Symbiosis in Aquatic
1646 Systems Initiative Investigator Award (GBMF9197; <https://doi.org/10.37807/GBMF9197>), a grant
1647 from the Simons Foundation (542395) as part of the Principles of Microbial Ecosystems (PriME)
1648 Collaborative, a grant (315230_176189) from the Swiss National Science Foundation, and support
1649 from the National Centre of Competence in Research (NCCR) *Microbiomes* (51NF40_180575).
1650 F.C.P. was supported by a Young Independent Research Group grant from the Austrian Science
1651 Fund (FWF; ZK-57). D.B. was supported by the Austrian Science Fund (FWF; P26127-B20 and
1652 P27831-B28), the United States Department of Energy (DE-SC0019012), and the European Research
1653 Council (Starting Grant: FunKeyGut 741623). Research in the lab of M.W. on Raman
1654 microspectroscopy and its application in microbial ecology was supported by an ERC Advanced
1655 Grant (Nitricare; 294343) and the Wittgenstein Award of the FWF (Z-383-B). W.E.H. acknowledges
1656 financial and instrumental support from EPSRC (EP/M002403/1, EP/M02833X/1) and NERC
1657 (NE/M002934/1). G.T. acknowledges support from NSF-MRI grant OCE-1336724 and a Gordon
1658 and Betty Moore Foundation Grant #5064. J.K. acknowledges funding by ERC Starting Grant
1659 259432 MULTIBIOPHOT. J.-X.C. acknowledges support from NIH (R35 GM136223 and
1660 R01AI141439).

1661 **Author contributions**

1662 Introduction (R.S., K.S.L. and Z.L.); Experimentation (R.S., K.S.L., Z.L., M.W., G.T.T., J.K., M.Z.
1663 and J.-X.C.); Results (R.S., K.S.L., Z.L., M.W., W.H., G.T.T., J.K., M.Z. and J.-X.C.); Applications
1664 (R.S., K.S.L., Z.L., F.C.P., M.W., D.B. and J.P.); Reproducibility and data deposition (R.S., K.S.L.
1665 and Z.L.); Limitations and optimizations (R.S., K.S.L., Z.L. and G.T.T.); Outlook (R.S., K.S.L. and
1666 Z.L.); Overview of the Primer (R.S., K.S.L. and Z.L.).

1667 **Competing interests**

1668 The authors declare no competing interests.

1669 **Peer review information**

1670 *Nature Reviews XXX* thanks [Referee#1 name], [Referee#2 name] and the other, anonymous,
1671 reviewer(s) for their contribution to the peer review of this work.

1672 **Supplementary information**

1673 Supplementary information is available for this paper at <https://doi.org/10.1038/s415XX-XXX-XXXX-X>

1674 **Related links**

1675 **KnowItAll:** <https://sciencesolutions.wiley.com/knowitall-spectroscopy-software/>

1676 **OptiFDTD:** <https://optiwave.com/optifdtd-overview/>

1677 **GAMESS:** <https://www.msg.chem.iastate.edu/gamess/capabilities.html>

1678 **ORCA:** https://www.orcasoftware.de/tutorials_orca/spec/IR.html#predicting-raman-spectra

1685 **List of Tables**

1686

1687 Table 1 | **Software packages for processing Raman microspectroscopy data in three common**
 1688 **programming languages.**

1689

Language	Useful libraries	Description	Licence
MATLAB	Supplementary File 1	A graphical user interface (GUI) platform that was designed in-house (developed by Lee, Landry & Stocker) for de-noising (based on the Savitzky–Golay algorithm) and baseline subtraction (based on polynomial fitting)	MathWorks ©; Libraries released here are under the MIT licence
Python	RamPy	Package for Raman data analysis, contains multiple options for pre-processing routines and some functions for downstream analysis	GPL2
	Scipy.signal	Implementation of Savitzky–Golay filtering and other signal processing routines	BSD
	peakutils	Functions for peak finding	MIT
	pywt	Library for wavelet transformations	MIT
	chemospec	Comprehensive package for chemometric data analysis, contains many options for pre-processing (baseline subtraction, smoothing) as well as advanced functions for downstream analysis.	GPL3
R	hyperspec	Family of packages for hyperspectral imaging data with a focus on biological applications. Also contains a number of parsers for common Raman data formats.	GPL3

1690

1691

List of Figures

Fig. 1 | **Raman working principle.** **a** | Three types of scattering signals that are generated as a result of interactions between light and a molecule. Rayleigh scattering does not change the wavelength of the scattered light, compared to the incident light. For Raman scattering, the wavelength of the scattered light is longer (Stokes) or shorter (anti-Stokes) than the incident light. **b** | A processed Raman spectrum of a single bacterium (*Vibrio alginolyticus*). The molecular composition of the cell can be identified from the individual peaks at different wavenumbers (indicated as Raman shift) that correspond to different molecular bonds. **c** | Energy level diagrams representing the generation of emission signals. Colours of the arrows represent the wavelength. For Rayleigh and Raman (Stokes and anti-Stokes) scattering, the molecule is excited to a virtual energy state and then returns to a lower energy level, accompanied by light scattering. In contrast, for resonance Raman scattering and fluorescence emission, the molecule undergoes a transition to a higher electronic state, generating a much stronger emission signal. Hyper-Raman relies on a nonlinear two-photon process. Coherent Raman scattering (CRS including CARS and SRS) is another type of nonlinear optical process based on the interaction between pump and Stokes lasers.

Fig. 2 | **Configuration of a Raman microspectroscopy system.** **a** | A fundamental Raman setup consists of components for bright-field light microscopy to select a region of interest for Raman measurements (a light source, a motorized *xyz*-stage, an objective and camera 1); a Raman laser to generate Raman signals from the sample (a beam expander is equipped to ensure that the laser beam fully fills the back aperture of the objective); optical components to deliver the generated Raman signals to the Raman system (beam splitters, mirrors, a Rayleigh filter, a confocal pinhole and a slit) and to divide the polychromatic Raman signal with respect to colour (a diffraction grating); and a detector to measure the Raman signal. The components marked with asterisks (*) require optimization in the choice of hardware and operational parameters to optimize Raman measurement. **b** | Integration of setups for epi-fluorescence detection and optical tweezers for optical trapping that can complement Raman interrogation of microbes. Implementation of a set of galvomirrors enables rapid area scanning for the Raman measurement. The components described in **a** are shown in grey.

Fig. 3 | **Sample preparation.** **a** | Measurements of dry cells (*Vibrio alginolyticus*) on an aluminium-coated slide provide greater sensitivity over those in liquid due to the absence of signals by the liquid medium, yet they usually require data processing to remove intrinsic backgrounds. **b** | For measurements of cells in liquid, use of a non-photo-luminescent medium is important, as shown in the difference in intensity between a sample in Luria-Bertani (LB) medium and 0.2M glycerol.

Fig. 4 | **Raman data processing.** **a** | Raw spectra can be directly used in a number of analyses, like direct measurement of peaks of interest with SIP. Raman spectra following SIP, where the carbon–deuterium peak ($2,040\text{--}2,300\text{ cm}^{-1}$) and the location shift of the C=C peak (from $1,660\text{ cm}^{-1}$ to $1,618\text{ cm}^{-1}$) indicate metabolic activity and carbon metabolism of microbes, respectively, during the incubation period. **b** | Raw data obtained from real Raman spectra from high-density cultures of three different bacterial strains (*Pseudoalteromonas* sp. 3D05, *Vibrio splendidus* 1A01, *Psychromonas* sp. 6C06). **c** | high-frequency noise is removed from the raw spectra using wavelet de-noising, followed by **d** | fitting of the baseline (shown here using asymmetric least-squares; dashed lines). **e** | The calculated baseline, arising from surrounding medium or substrates is subtracted to provide an approximation of the pure spectra (presenting the cells). **f** | The simplest example of an unsupervised multivariate analysis is principal component analysis (PCA), which emphasizes differences among samples by fitting a new set of orthogonal axes along the directions of maximum variance in the dataset ($n = 32$ for each species, substrate is a glass/PDMS microfluidic device for panels **f–i**). Ellipses represent 95% confidence intervals for each group. **g** | Self-organizing maps (SOM) are a slightly more advanced unsupervised technique in which a two-dimensional grid of nodes, each representing an archetypal

1744 data point occupying some volume of the underlying multivariate space, is stochastically trained to fit the
1745 dataset such that closed-related nodes group together. Here, the circles indicate nodes ($n = 16$). The colour
1746 indicates that the node is substantially occupied by one of the corresponding bacterial species or the substrate.
1747 White nodes represent null spaces and bold lines represent borders separating the nodes of each group. **h** |
1748 Support vector machines (SVM) divide a multivariate space into is and is not volumes for a group of interest.
1749 In this example, the hyperplane represents the decision boundary of a SVM trained to identify *Psychromonas*
1750 *sp.* 6C06. **i** | Linear discriminant analysis (LDA) is a straightforward classification technique. Tight clustering
1751 of points in the trained space show the new axes are fitted to simultaneously maximize among-group variance
1752 while minimizing within-group variance.

1753
1754

1755 **Fig. 5 | Raman data interpretation. a** | Raman spectra of a *Bacillus cereus* endospore and vegetative cell.
1756 The peaks at 824, 1,017, 1,395, 1,446, and 1,572 cm^{-1} correspond to CaDPA, which accumulates in the
1757 endospore. **b** | Resonance Raman spectra of a non-photosynthetic bacterium (orange), *Synechocystis* sp.
1758 PCC6803 (green), and pure beta-carotene (blue). The three peaks at 1,001–1,007, 1,154–1,156, and 1,511–
1759 1,517 cm^{-1} correspond to carotenoids. **c** | Comparison of Raman spectra from a carotenoid-containing
1760 *Symbiodinium* CCMP421 microalga (red) and a carotenoid-lacking *Vibrio alginolyticus* bacterial cell (blue).
1761 The high level of background in the *Symbiodinium* spectrum corresponds to fluorescence signals that
1762 accompany the resonance Raman scattering. **d,e** | SIP–Raman spectral analyses of isotopic signatures of
1763 photoautotrophs grown on ^{13}C -bicarbonate. **d** | Resonance Raman spectra of single *Synechococcus* sp. cells
1764 from cultures grown on natural ^{13}C abundance (1.1% ^{13}C) (colour; Dominique, please correct — bottom
1765 spectrum) and from a culture in 54% ^{13}C media after 3 (colour; same here — second bottom), 6 (colour; same
1766 here — third bottom), 12 (colour; same here — second top), and 24 (colour; same here — top spectrum) days
1767 of growth. Vertical lines indicate major peak positions in the 1.1% ^{13}C culture. **e** | Curve-fitting analysis of
1768 isotopic signatures of an *Emiliana huxleyi* cell (Prymnesiophyceae) with a calculated $65 \pm 7\%$ ^{13}C content.
1769 Raman spectral region around the four isotopologue peaks for the phenylalanine ring breathing mode (red,
1770 measured using a 633 nm laser after chemiphotobleaching to suppress autofluorescence). After baseline
1771 correction and normalization, contributions of each isotopologue was determined by curve deconvolution and
1772 peak fitting (blue) to yield the lower spectrum¹²³. In the molecular structures, ● represents ^{13}C substitutions in
1773 the phenyl ring⁷⁷. **f–h** | FISH–Raman for microbes in groundwater. **f** | FISH images of bacterial cells
1774 hybridised with EUB338 (purple) and specific probes for *Acidovorax* sp. (Cyanine 3-labeled probe, red) and
1775 *Pseudomonas* sp. (fluorescein isothiocyanate probe, green). Scale bar: 10 μm . **g** | Several bands of Raman
1776 spectra of individual bacteria shifted as they integrated ^{13}C -naphthalene upon incubation in minimal media
1777 supplemented by ^{13}C -naphthalene as the sole carbon source (colour; Dominique, please correct), in contrast
1778 to medium supplemented with ^{12}C -naphthalene (colour; Dominique, please correct). **h** | Correlation between
1779 ^{13}C -naphthalene content and red shift of the bacteria ($I_{967} / I_{1,003}$). **i** | SERS and SEHRS spectra of adenine (50
1780 μM) obtained using nanoaggregates from hydroxylamine-reduced silver nanoparticles. SERS enabled the
1781 measurement with high sensitivity and SEHRS revealed additional peaks that are not visible in SERS or
1782 normal Raman scattering. **j** | SRS images of deuterium-labelled *Pseudomonas aeruginosa* cells among
1783 (unlabelled) blood cells. Images with respect to the C–D (2,168 cm^{-1}) and C–H (2,915 cm^{-1} ; representing
1784 mainly proteins) peaks represent *P. aeruginosa* only and both types of cell, respectively. Scale bar: 5 μm .
1785 Panel b adapted from ref. ⁷⁶. Panel c adapted from ref. ⁶¹. Panel d adapted from ref. ⁶⁸. Panels f–h adapted from
1786 ref. ¹²⁸. Panel i adapted from ref. ¹³². Panel j adapted from ref. ¹³⁶.

1787
1788

1789 **Fig. 6 | Applications of Raman-based cell sorting to link ecological roles of microbes to their genomic**
1790 **identities. a** | Marine microbial cells displaying resonant carotenoid Raman bands (or ^{13}C -induced shifts in
1791 carotenoid bands due to incorporation of ^{13}C -bicarbonate) were sorted and their genomes amplified and
1792 sequenced. This led to the identification of novel organisms involved in carbon fixation in the ocean, as well
1793 as novel genes for carotene synthesis^{116,117}. **b** | Mouse gut bacteria that are metabolically active when
1794 supplemented with mucin or mucosal sugars were labelled using D_2O and sorted based on the C–D peak
1795 (2,040–2,300 cm^{-1}) using optical tweezers, enabling the identification of a consortium of mucosal sugar

1796 utilizers able to counteract the pathogen *C. difficile*^{63,69,70}. **c** | Microalgal or yeast cells accumulating large
1797 amounts of commercially attractive compounds such as the carotenoid astaxanthin or triacylglycerols were
1798 sorted based on characteristic Raman peaks, after encapsulation into individual droplets^{72,164}. This allowed
1799 rapid screening and retrieval of microbial cell factories hyper-producing compounds of interest, as well as to
1800 the identification of novel genes encoding key enzymes in their synthesis⁷².

1801

1802

1803 **Fig. 7 | Use of SERS tags for the quantification of the pathogen *Staphylococcus aureus* in different**
1804 **biofluids. a** | Illustrations of the conventional method in which samples from different fluids are spread on
1805 blood agar plates and cultured before quantification of the number of colony-forming units (CFU). **b** |
1806 Quantification of the pathogen for 20 min using SERS tags in an engineered microfluidic device. The SERS
1807 signals were measured in the middle of a straight channel where the sample fluid was introduced. The
1808 measured SERS spectra were normalized by a reference SERS spectrum. **c** | Comparison between estimates of
1809 pathogen concentration based on cell culture (red circles) and based on SERS tags (cyan squares). Filled
1810 symbols show the averages over three replicates. Adapted from ref. ¹⁸³.

1811

1812

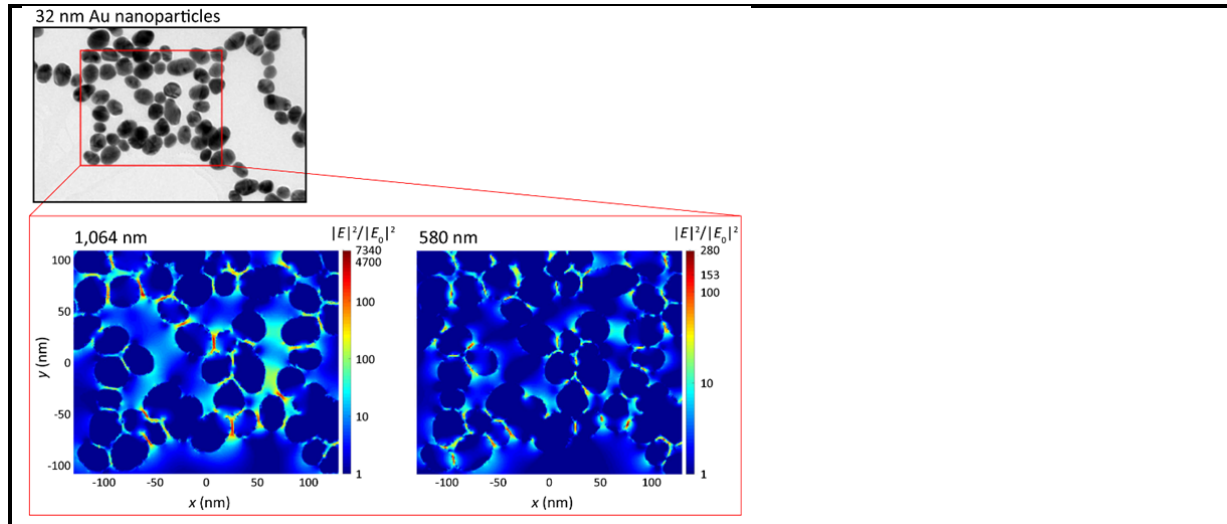
1813

List of Boxes**Box 1 | Underlying mechanisms for SERS**

SERS relies on electromagnetic and chemical enhancements, increasing Raman signal intensities by up to 10^8 – 10^{14} orders of magnitude²⁹. The former arises from localized surface plasmon resonance (LSPR). When metallic nanoparticles are excited by a laser used to generate Raman scattering, their electrons perform collective oscillations, inducing a dipole in the individual nanoparticles. The field of this induced dipole causes strong enhancement of the electromagnetic field of the excitation, thereby intensifying Raman signals generated from the molecules in this field^{233,234}. This electromagnetic enhancement peaks at the nanoparticle surface and exponentially decays with distance r — proportional to r^{-12} (ref. ²³⁴). Care should be taken when applying SERS for the interrogation of microorganisms because the electromagnetic enhancement effect is confined to the proximity of the metallic nanoparticles, leading to potential issues, for example, limited reproducibility arising from variation dependent upon the orientation of the sampled microbe with respect to the SERS substrate²³⁵. Additionally, the SERS signal of microbes is strongly influenced by the secretion of compounds like nucleotides or degradation products upon starvation and osmotic stress^{37,38}.

Chemical enhancement of the signal arises from physico-chemical interaction between molecules and the metallic nanoparticles. The generated Raman signal is intensified when the wavelength of the laser illumination is resonant with the charge transfer states between the metal and the molecules. This effect occurs only when there is a very short distance between the metal and molecules.

The laser wavelength providing SERS functionality depends on the metallic nanoparticles used. Gold and silver nanoparticles generate SERS effects for 570–1,230 nm and 400–1,000 nm lasers, respectively²³⁶. Additionally, the size of the metallic nanoparticles determines the optimal wavelength that generates maximum SERS enhancement. The illustration below (adapted from ref. ²³⁷) show that the electric field can be enhanced in the presence of gold nanoparticles with size of 32 nm ($|E|^2/|E_0|^2$, where E and E_0 are the electric fields in the presence and absence of gold nanoparticles, respectively) and that the enhancement of the electric field in the vicinity of gold nanoparticles is more than 20 times greater with the excitation of a 1,064-nm laser than with a 580-nm laser.



1816

1817

Box 2 | **Optimization of technical components.**

Optimization of technical parameters is required to obtain a Raman signal of sufficient intensity to allow reliable and precise measurement. Here, we outline six important aspects to be considered in the setup of the hardware and the operation of a Raman system. For more detailed information on these, see **Supplementary Note 1**.

Microscope

Upright or inverted microscopes can be considered depending on the application. Hardware for additional functionalities, such as phase contrast or differential interference contrast microscopy, is compatible with Raman measurement, yet specific optical components for those systems, like a phase ring at the rear focal plane of an objective, could reduce Raman signals.

Confocality

Specifications of the objective and its combination with a confocal setup within the Raman system must be chosen so that the interrogation volume is appropriate for the size of the microbes of interest. General recommendations are difficult to provide, rather the confocality should be assessed experimentally.

Detector

An appropriate detector must be chosen on the basis of its quantum efficiency. In general, front-illuminated charge-coupled device (CCD) detectors provide a good price–performance ratio, whereas back-illuminated CCD detectors can be considered for measurements requiring higher sensitivity.

Laser

The wavelength of the laser has a considerable impact on the generated Raman signals. The shorter the wavelength used, the stronger the generated Raman, but also the higher the likelihood of generating fluorescence signals that interfere with measurement of the Raman signals. Given this trade-off, 532 nm is recommended as a starting point.

Substrate

Raman signals from the substrate holding the sample are usually of comparable or higher intensity than those from the sample. Glass slides or coverslips can be used as a starting point for measurements of novel samples. If a substrate with less background in the spectral region of interest is required, other materials like aluminium, calcium fluoride or quartz can be used.

Diffraction grating

A key component in the determination of the spectral resolution of the measured Raman spectra. A grating that can measure a phenylalanine peak at $1,007\text{ cm}^{-1}$, the sharpest of the peaks among biologically important compounds can be considered as a default setup. The higher the grating number, the greater the spectral resolution but the lower the diffraction efficiency.

Box 3 | **Fluorescence *in situ* hybridization (FISH)**

FISH with 16S or 23S rRNA-targeted oligonucleotide probes enables microbiologists to specifically stain microbes of interest in complex samples²³⁸ and to quantify their abundance and ribosome content in environmental and medical samples²³⁹. The signal intensity of FISH reflects the ribosome content of the cells and is thus dependent on their activity. The detection of cells with low ribosome content can be achieved using catalyzed reporter deposition (CARD)–FISH that strongly enhances the FISH signal²⁴⁰, but requires the application of a more time-consuming protocol.

Several different fluorophores have been used for FISH in microbial communities, allowing for the simultaneous detection of multiple taxa with different probes^{241–243}. The combination of FISH and Raman microspectroscopy enables researchers to record Raman spectra of selected microbes of interest in a complex community in a targeted manner and has successfully been applied for stable isotope labelling experiments⁷⁰ or for the detection of storage compounds¹³⁰ in selected taxa. Ideally, for FISH–Raman, fluorophores should be selected that are not excited by the applied Raman laser, yet bleaching the dyes after their measurement provides an alternative^{62,81}.

It should be kept in mind that the fixation and permeabilization steps as well as the hybridization and wash steps of the FISH protocol can cause loss of biomolecules from the stained cells and thus decrease the Raman signal of storage compounds or lipids. The latter has been shown to slightly reduce the deuterium signal in FISH–Raman experiments after stable isotope probing (SIP) with heavy water⁷¹.

1819

1820

Box 4 | Tracer selection.

In designing a SIP experiment, it is ideal to use tracer substrates that are uniformly labelled with one or more of the four small stable isotopes (^2H , ^{13}C , ^{15}N , ^{18}O).

Carbon

Carbon is the most commonly chosen isotope because it comprises about 47–50% of cellular mass²⁴⁴. Several vibrational modes produce distinctive Raman peaks for different isotopologues that can be used to calculate fractional isotopic abundance ($f_{\text{cell}} = ^{13}\text{C} / (^{13}\text{C} + ^{12}\text{C})$) in a particular moiety or an entire cell. For example, the ring breathing modes of purines, pyrimidines and the essential amino acid phenylalanine, and vibrational modes emanating from carotenoids of photoautotrophs are all useful reporters of ^{13}C assimilation^{62,68,75}.

Deuterium

Deuterium is a versatile tracer for SIP–Raman experiments. Deuterated tracers (like deuterium-labelled dimethylsulfoniopropionate, DMSP) can be used to track substrate assimilation and to unravel biosynthetic pathways^{62,126,245–247}. Alternatively, amending the medium with 10–50% (vol/vol) D_2O enables identification of all metabolically active cells after brief incubation. The clear advantage of the D_2O approach is that the investigator need not make any supposition about which substrates support microbial growth. Furthermore, unlabelled substrates or antagonists of interest can be added together with D_2O to screen for substrate-induced stimulation or inhibition of growth of microbial taxa⁶⁹. Additions of D_2O with concentrations up to 50% (vol/vol) reportedly do not strongly inhibit growth of tested bacterial strains⁷⁰. D_2O can have subtle effects on microbial growth even at much lower concentrations^{248–250}.

Nitrogen

Use of SIP–Raman to track the movement of nitrogen ($^{15}\text{NH}_4^+$, $^{15}\text{NO}_3^-$, $^{15}\text{N}_2$) from dissolved pools through individual cellular pools is challenging because N comprises only about 14–16% of cellular mass²⁴⁴. Raman shifts caused by ^{15}N replacement can overlap with neighbouring Raman bands and maximal spectral shifts between the 100% ^{14}N and 100% ^{15}N isotopologues are only 13–17 cm^{-1} (refs. ^{78,80}). SERS has been employed to measure $^{15}\text{N}_2$ fixation by cultured diazotrophs with improved sensitivity⁷⁸, yet care should be taken considering the potential limitations of SERS for adoption in microbiology.

Oxygen

Similar to using D_2O , H_2^{18}O can be used as a general tracer of anabolic activity. SIP–Raman experiments with a H_2^{18}O tracer combined with 2D correlation analysis have been used to track protein synthesis and DNA replication in single cells through all bacterial growth phases²⁵¹.

1821

1822

Box 5 | RACE/RACS/RADS

Raman-based cell sorting systems consist of hardware for Raman measurement of individual microbes and for sorting cells of interest based on mechanical, optical, electrical or magnetic force (reviewed in refs. ^{146,252}). The system configuration determines two key features: sorting throughput and the type of microbes that the system can handle. Here, we outline three designs: Raman-activated cell ejection (RACE), Raman-activated cell sorting (RACS), and Raman-activated droplet sorting (RADS).

RACE

Microbes are immobilized on a slide and cells of interest are identified on the basis of Raman measurements. The slide is inverted and transferred to a laser microdissection system so that cells of interest can be ejected towards a collection chip below²⁵³. The device has been engineered such that the sample is loaded at the bottom surface of the slide, so that identification and ejection of cells of interest can be performed without moving the slide¹¹⁷. RACE enables sorting of ~200–300 cells/day without limitations on the type of microbes for sorting.

RACS

Integration of optical tweezers into a fluidic system provides a means to immobilize cells within the Raman interrogation volume during measurement, boosting the precision of Raman measurement, and then translocate those cells for collection. Raman and optical tweezers were operated manually within a glass capillary in which one end was filled with a sample and then cells of interest were translocated to buffer medium at the other end⁷⁰. In a new version, an automated fluidic system is integrated, increasing sorting throughput from 1–2 cells/h to up to 500 cells/h and reducing the need for human intervention^{61,63,69}.

RADS

Encapsulating single cells of interest within individual droplets allows spatial isolation of those cells, facilitating a pipeline for single-cell genomics²⁵⁴. Cells of interest are searched and identified in still fluid based on Raman measurement, individually encapsulated and sorted, and then used for genomics. This process is known as Raman-activated gravity-driven encapsulation and sequencing; RAGE-Seq⁷¹. Encapsulation of individual cells also facilitates rapid dielectrophoretic sorting of the single-cell droplets in conjunction with a fluidic device⁷². The former approach⁷¹ is applicable for sorting of diverse types of microbes (with throughput of 2 cells/min), whereas the latter⁷² has been demonstrated using relatively large cells (10- μ m fungi and throughput of 40–120 cells/min).

1824 **Glossary**

1825

1826 **Fourier transform infrared (FTIR) spectroscopy**

1827 The other prominent method of vibrational spectroscopy, where absorption of light by a sample
1828 (instead of scattering as in Raman microspectroscopy) is used to identify the molecular composition
1829 of the sample

1830

1831 **Spectroscopy/microscopy**

1832 In this Primer, ‘spectroscopy’ indicates a technique involving point measurement of a sample across
1833 a wide spectral region (applied to most Raman systems described in this Primer), whereas
1834 ‘microscopy’ refers to imaging of spatial region of interest with respect to a single wavenumber
1835 (applied to coherent Raman)

1836

1837 **Wavenumber**

1838 A unit of frequency used in vibrational spectroscopy, defined as the frequency divided by the speed
1839 of the wave and thus equal to the number of waves within one centimetre (cm^{-1})

1840

1841 **Normal Raman microspectroscopy**

1842 A fundamental form of Raman microspectroscopy that relies on measurement of non-resonant,
1843 spontaneous scattering signals in which one out of $\sim 10^6$ incoming photons to a sample is scattered

1844

1845 **Resonance Raman scattering**

1846 Raman scattering that arises when the wavelength of the incident laser beam matches the electronic
1847 transitions of a molecule, which generates much more intense Raman signals than normal Raman
1848 scattering

1849

1850 **Raman reporter**

1851 A chemical that generates a known SERS signal

1852

1853 **Mode-locked laser**

1854 A laser that produces ultrashort pulses on the picosecond or femtosecond scale

1855

1856 **Selection rule**

1857 Constraints that govern the likelihood whether undergoing particular quantum transitions from one
1858 state to another is allowed or forbidden

1859

1860 **Beating frequency**

1861 Frequency difference between two electromagnetic waves that interfere constructively and
1862 destructively

1863

1864 **Spectral window**

1865 A spectral region of interest

1866

1867 **Diffraction grating**

1868 A glass plate etched with very close parallel lines that produces a spectrum from a coherent light
1869 beam by diffraction and interference of light and thus functions as a planar prism

1870

1871 **Chromatic aberration**

1872 Discrepancy of focus in axial and transverse directions between rays with different wavelengths after
1873 a focusing lens due to the discordance of their refraction angles

1874

1875 **Galvomirror**

1876 A pair of mirrors, each of which is integrated with a rapidly moving scanning motor, which enables
1877 enlargement of a laser beam spot to a small scanning area

1878

1879 **Dichroic mirror**

1880 An optical component for fluorescence microscopy by which monochromatic light for the excitation
1881 of fluorophores in a sample is separated from generated fluorescence signals

1882

1883 **Isotopologues**

1884 Molecules that are structurally identical yet differ from one another by the presence of at least one
1885 atom possessing a different number of neutrons

1886

1887 **Uniformly labelled tracer**

1888 All available positions in a molecule for a given element are occupied by an isotopically heavy or
1889 radioactive nuclide, typically noted as ${}^n\text{E}-(\text{U})$ -compound, where n = atomic mass, E = elemental
1890 symbol, U = uniformly, followed by chemical form

1891

1892 **Fractional isotopic abundance**

1893 The proportion of atoms in a molecular pool populated by the heavy isotope – also referred to as
1894 atom% (multiplied by 100) in literature

1895

1896 **Biomolecular fingerprint**

1897 An indicator in which chemical properties of a biomolecule are encoded – in vibrational
1898 spectroscopy, collective vibrational frequencies in wavenumber of chemical bonds within a
1899 biomolecule

1900

1901 **Raman-silent**

1902 The absence of Raman-active vibrational modes

1903

1904 **Savitzky–Golay filter**

1905 A filter algorithm that fits a polynomial of a known order to each point in the spectrum, using a
1906 sliding window of a user-defined width, subsequently replacing each point with the fitted value at the
1907 centre of the window

1908

1909 **Vector normalization**

1910 A normalization approach in which the intensity at each wavenumber is divided by the square root of
1911 the sum of squares of intensities for all wavenumbers within a spectral window, such that the
1912 Euclidean distance from the origin in the multidimensional space is equal to 1

1913

1914 **Mahalanobis distance**

1915 A measure of the distance between a point and the centroid of a multivariate normal distribution, in
1916 units of standard deviations

1917

1918 **Non-negative matrix factorization**

1919 A technique that represents each point in a set of mixed spectra as a weighted mixture of a finite
1920 number of conserved sub-spectra, with the axes being directly interpretable as Raman sub-spectra

1921

1922 **Independent component analysis**

1923 A technique that optimizes a new set of axes to naively capture covariance between variables
1924 separately for each of a finite number of independently varying subsets of data

1925

1926 **Isotopomers**

1927 Isotopomers of a compound have the same number of each isotope, but their positions differ

1928

1929 **Voigt probability distribution profile**

1930 A convolution of Gaussian and Lorentzian probability distributions that is widely used in peak-fitting
1931 routines to describe the symmetry of peaks in Raman spectroscopy